Université de Genève
Département de Physique
de la Matière Condensée

Faculté des Sciences
Professeurs J.-M. Triscone et P. Paruch

Studies of magnetoelectric coupling in $BiFeO_3$-$CoFe_2O_4$ nanocomposites

Travail de Master

présenté à la Faculté des Sciences
de l'Université de Genève

par

Jill Guyonnet

Directeurs de travail : Prof. J.-M. Triscone, Prof. P. Paruch
Assistante : Dr. C. Lichtensteiger

Juin 2008

Acknowledgements

This master thesis was done in the Department of Condensed Matter Physics, in the University of Geneva, and I wish to dedicate a few lines to thank every person who as helped and encouraged me during these months.

I wish to thank Prof. Jean-Marc Triscone, first for introducing me to the realm of experimental condensed matter physics by offering me a summer internship in his group, and then for offering me such an exciting project for my master thesis.

I thank Prof. Patrycja Paruch for accepting to be my other work advisor, for her patience in proofreading and for the incredible amount of advice.

My recognition also goes to Dr. Enrico Giannini, for accepting to be part of the jury with such short notice.

I warmly thank Dr. Celine Lichtensteiger for her enthusiastic help, proofreading and advice in the oral defense.

Many thanks go to all members of the Triscone and Paruch groups for their help and good mood.

I also wish to thank Prof. Josep Fontcuberta, Dr. Florencio Sánchez and Nico Dix, for this exciting collaboration and enthusiastic discussions.

A special thank to Elisabeth Agoritsas, for reading this work with an external (and pertinent) eye and for supporting me in the stress of the last weeks.

I also thank my former classmates, for these years of common struggle and mutual help through university.

Finally, I thank my family and friends, who showed both interest for my work and great support during the stressful times.

Contents

Chapter 1

Introduction

Understanding the electric and magnetic properties of solid, and especially crystalline materials has been the driving force of condensed matter physics, both for modern technological applications and for fundamental physics investigation. One technological application concerns data storage. In order to encode binary bits, materials used for memories need to have two non-volatile and rewritable states. Ferroic materials, in particular ferromagnetic and ferroelectric materials, have proven particularly useful in current memories.

Ferromagnetic materials exhibit two stable and opposite states of spontaneous magnetization that can be reversed by a suitable magnetic field. Regions of uniform magnetization known as domains can therefore be used to encode binary bits. In the past decade, advances in atomic- and nanoscale growth and characterization techniques have led to the study and exploitation of a range of new magnetic phenomena related to the spin of electrons in addition to their well known charge properties. Examples include colossal and giant magnetoresistive materials, in which magnetic fields cause order of magnitude changes in conductivity. Some technological applications such as sensors, read-heads and memories based on on giant magnetoresistive materials are already commercially available, while many other proposed technologies, such as spin valves and spin transistors, are still under development.

Ferroelectric materials exhibit two stable and opposite states of spontaneous electrical polarization that can be switched by a suitable electric field. In parallel with ferromagnetic materials, they are useful for memory applictions. Ferroelectrics are also pyroelectric, which means that their dipolar moment is temperature dependent, and piezoelectric, responding with an electric potential to applied mechanical stress and vice versa. In addition to ferroelectric random access memories (FeRAM), ferroelectrics are therefore used in a range of technological applications, including transducers, actuators and capacitors (because of their high dielectric permittivity). The diverse electrical properties and complex phase diagram of ferroelectric oxides also make them interesting from the point of view of fundamental physics, for instance as a model system for studying the effects of disorder or thermal evolution.

Especially interesting for technological applications as well as fundamental research are materials in which both types of behavior can be combined. Materials that are simultaneously ferroelectric and ferromagnetic belong to a class known as multiferroic materials, and have all the potential for use in technological applications of both their parent materials. Moreover, since the coexistence of these two orders could potentially alow their cross-coupling through the mag-

netoelectric effect, an extra level of complexity in their fundamental physics and a whole range of new functionalities can be envisaged. Applications include multiple-state memory elements, in which data can be stored both ferromagnetically and ferroelectrically, and novel memory media, which could allow ferroelectric data writing to be combined with ferromagnetic reading.

However, experimental development has shown that the conditions for coexistence of ferroelectricity and ferromagnetism are rarely met in single-phase materials. Alternative routes to producing multiferroics materials have therefore been explored, including composite systems made of a ferroelectric and a magnetic phase coupled to each other via epitaxial strain. This work reports on local probe studies of magnetoelectric coupling in such a system, in which bismuth ferrite ($BiFeO_3$) and cobalt ferrite ($CoFe_2O_4$) play the role of the ferroelectric and magnetic phase respectively. The samples were grown by N. Dix from the group of J. Fontcuberta, in ICMAB, Bellaterra, Spain.

This report is structured as follow: theoretical basis relevant to multiferroic materials are firstly reviewed. Structural properties of the consitutent phases and experimental details are then presented. Finally, a surface and magnetic characterization of the samples is reported along with the set of experiments performed to highlight the possible magnetoelectric coupling.

Chapter 2

Theoretical elements

2.1 Overview

A brief review of the role of symmetries in phase transitions through Landau theory and of the phenomenologies of magnetism and ferroelectricity is given in this section.

2.1.1 Symmetry and ordered phases

Symmetry is of prime importance in the realm of condensed matter physics, for it is closely connected with the hypothesis that certain physical quantities are unobservable, and its direct consequences, explained by Noether's theorem, are the conservation laws or selection rules. Possible examples are listed in [2].

A thermodynamic phase transition is the transformation of a thermodynamic system from one phase to another due to competition between an ordering energy and entropy[1]. It is signalled by a singularity in a thermodynamic potential, such as the Helmholtz free energy $F = U - TS$. If there is a finite discontinuity in one or more of the first derivatives of the appropriate thermodynamic potential, the transition is termed first-order; a jump in the entropy S implies that the transition is associated with a latent heat. If the first derivatives are continuous but second derivatives are discontinuous or infinite, the transition is termed second-order, and corresponds to a divergent susceptibility.

Landau's theory of second-order phase transitions introduces the concept of broken symmetry, which may be summarized as the sudden disappearance, below a critical temperature T_c, of a certain symmetry element present in the high-symmetry phase and the appearance of an ordered phase, with the value of a certain order parameter[2] ψ being different from zero. It is based on the assumption that, in the vicinity of the phase transition point where ψ becomes arbitrarily small, the free energy of the system F can be expanded in a power series of ψ, where

[1] Other kinds of phase transitions exist, such as the inter-particle interaction driven metal-insulator phase transition in Mott insulators.

[2] The order parameter may be a scalar, a vector, a complex number or a more complicated quantity. For the purpose of simplicity, we will take it to be a scalar in the present demonstration.

only those terms compatible with the symmetry of the system are included[3]:

$$F = F_0 + \sum_n \alpha_n \psi^n, \tag{2.1}$$

where F_0 is the free energy of the high symmetry phase and unrelated to the phase transition, and the α_i are pressure and temperature dependent parameters.

The stability condition requires that $F(\psi)$ be a minimum for the equilibrium value of ψ:

$$\left(\frac{\partial F}{\partial \psi}\right)\Big|_{\psi_{equ}} = 0, \quad \left(\frac{\partial^2 F}{\partial \psi^2}\right)\Big|_{\psi_{equ}} > 0. \tag{2.2}$$

For $T > T_c$, the equilibrium value is $\psi = 0$ so that $\alpha_1 = 0$ and $\alpha_2 > 0$; for $T < T_c$, ψ takes a non-zero value so that $\alpha_2 < 0$. Therefore, $\alpha_2 = 0$ at the transition point and in the vicinity of T_c, α_2 may be written as a linear function of temperature:

$$\alpha_2(T) = \tilde{\alpha}_2(T - T_c). \tag{2.3}$$

If we now restrain our consideration to the case where the two possibilities of broken symmetry for ψ and $-\psi$ are equivalent, even power terms are the only ones that survive in the free energy expansion. Generally, α_4 is weakly temperature dependent and may be taken as a positive[4] constant. The free energy may then be written:

$$F = F_0 + \tilde{\alpha}_2(T - T_c)\psi^2 + \alpha_4\psi^4, \tag{2.4}$$

where the series can be truncated after the term $O(\psi^4)$, because if $a_4 > 0$, subsequent terms cannot alter the critical behavior of the system [3].

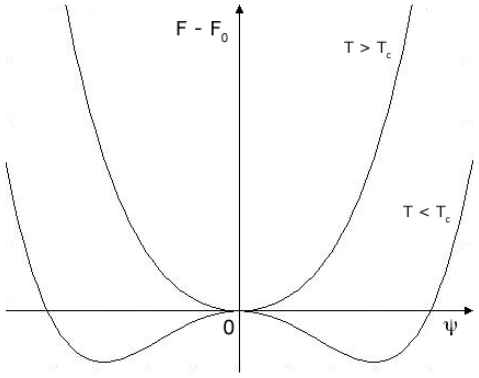

Figure 2.1: Free energy vs. order parameter in the vicinity of the second-order phase transition.

Figure 2.1 shows $F - F_0$ plotted as a function of ψ for $\alpha_4 > 0$. For $T < T_c$, two stable states corresponding to a finite value $\pm\psi_0$ exist as a consequence of the physical symmetry assumed above, yielding the so-called *double-well potential*.

Landau theory can be extended to treat some weak first-order phase transitions. The most common example is the contribution of an applied field h, which leads to an additional term $-h\psi$ in the free energy:

$$F_h = F_0 + \tilde{\alpha}_2(T - T_c)\psi^2 + \alpha_4\psi^4 - h\psi. \tag{2.5}$$

[3]Landau's theory considers the Helmoltz free energy F; instead, one can also expand the Gibbs free energy $G(p, T, \psi)$ to get pressure and temperature dependent coefficients.

[4]This corresponds to the physical condition that ψ must be bounded.

Figure 2.2 shows that the free energy becomes asymmetric about ψ. Also the minimum of free energy above T_c is not at $\psi = 0$, and below T_c the two minima are not equal.

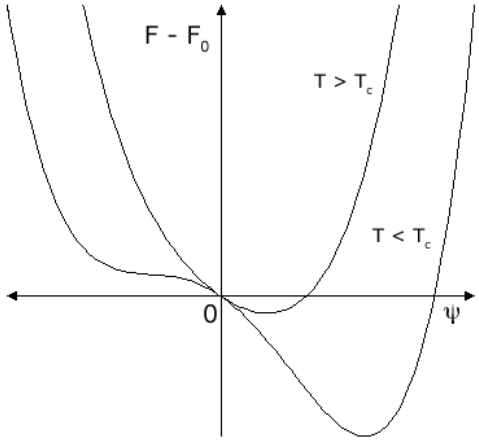

Figure 2.2: Asymmetric free energy under external field.

By using the equilibrium condition $\partial F_h/\partial\psi = 0$, we have the equation of state

$$2\tilde{\alpha}_2(T - T_c)\psi + 4\alpha_4\psi^3 - h = 0. \tag{2.6}$$

Figure 2.3 shows ψ as a function of h for $T < T_c$, $T = T_c$ and $T > T_c$. The solid lines refer

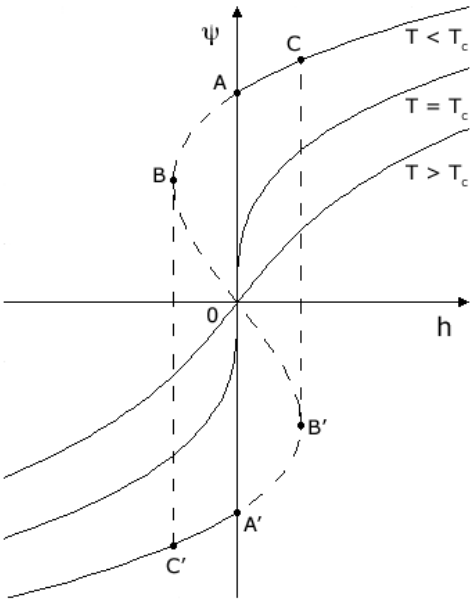

Figure 2.3: Order parameter as a function of external field at constant temperature.

to stable and the dashed lines to unstable states of the system. The segments A-B and A'-B' correspond to metastable states, while the segments B-O and B'-O' refer to unstable states with $\partial^2 F/\partial h^2 < 0$. Therefore, when h is varied, ψ and F exhibit discontinuities between the states corresponding to the points B-C' and C-B', yielding a *hysteresis loop* C-A-B-C'-A'-B', with a coercive field equal to $(h_{B'} - h_B)/2$.

2.1.2 Magnetism

Magnetic behavior in solids involves, in general, the orientation of magnetic dipoles, which are composed of the electronic spins and orbitals[5], and, according to its magnitude and sign, principally includes five types: diamagnetism, paramagnetism, ferromagnetism, antiferromagnetism and ferrimagnetism (see figure 2.4). While the former two represent the properties of the independent moment ensemble, the latter three reflect cooperative phenomena of a large number of moments. Details can be found, for instance, in [1] or [2]. Other spin configurations such as helical, canted or spiral ordering also exist, and, as we shall see in section 2.3.3, can induce non-trivial critical properties.

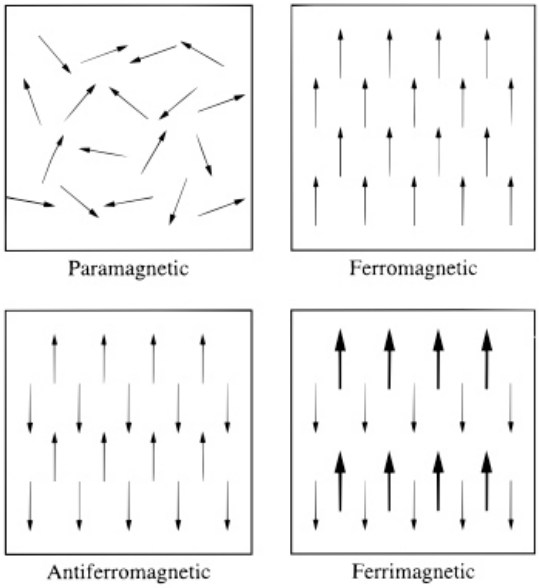

Figure 2.4: Common examples of magnetic dipole ordering, from [9].

Magnetic ordering, such as ferromagnetism, arises from the broken symmetry of time-reversal or spin-rotation. It is therefore described macroscopically in Landau theory with the amount of magnetic moments per unit volume, termed *magnetization* $\vec{M}$, being the order parameter. Under the application of an external field, the magnetization exhibits a hysteretic behavior as illustrated in figure 2.5.

Ferromagnetism originates microscopically from the exchange interaction, which favors parallel spin alignment at short length scales. At long distances, the exchange energy advantage is overtaken by the classical tendency of dipoles to anti-align. In non-magnetized ferromagnetic materials, the dipoles in the whole material are therefore not aligned but tend to organize in magnetic *domains* known as Weiss domains. The transition between two domains, each with a different magnetization orientation, is called a *domain wall* (termed Bloch or Néel wall, depending upon whether the magnetization rotates parallel or perpendicular to the domain interface) and is a gradual transition on the atomic scale (covering a distance of about 300 ions for iron). Domain re-orientation parallel to the external magnetic field is reponsible for the

[5] As the nuclear magnetic moment is smaller than the electronic moment by three orders of magnitude, it can be neglected when investigating macroscopic magnetism in solids.

hysteretic behavior of $M(H)$.

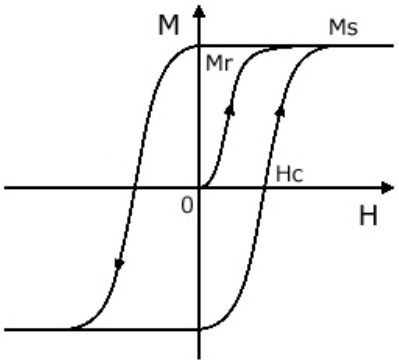

Figure 2.5: Hysteresis loop for a ferro- or ferrimagnet. As the magnetic field H is increased from zero, the magnetization M reaches a saturation value M_s; when H is brought back to zero, M reaches a remanent value M_r; the coercive field H_c is defined as the field value to bring M to zero.

The hysteretic magnetic behavior in ferromagnets has been exploited in numerous technological applications, such as data storage using regions of opposite magnetization, or magnetic circuits in transformers. However, such devices present a number of shortcomings, including the necessity of producing sufficiently large and increasingly local magnetic fields for magnetization switching, which leads to high power consumption and output. Also, the continuing demand for ever higher information densities results in increasingly complex device architecture and fabrication.

2.1.3 Ferroelectricity

Phenomenology. Ferroelectrics are crystals that possess a spontaneous electric polarization $\vec{P}$ which can be hysteretically reversed by applying a suitable electric field (see figure 2.6). This spontaneous polarization disappears above a critical temperature T_c, at which the system undergoes a structural phase transition to a higher symmetry (paraelectric) phase. The presence of two stable states has led to the integration of ferroelectrics, like ferromagnets, in information storage applications, such as the random access memories (RAM) used in *Playstation II* or smart cards[6]. However, a major drawback of ferroelectric RAM (FeRAM) is the destructive nature of the read-out process, which requires the measured region to be re-written each time it is accessed.

Macroscopic description. In many ferroelectrics, both second-order and weak first-order transitions have been experimentally observed. Devonshire therefore extended Landau's theory by expanding the free energy to the sixth order:

$$F = F_0 + \alpha_2 P^2 + \alpha_4 P^4 + \alpha_6 P^6, \tag{2.7}$$

where $\alpha_4 > 0$ for a second-order phase transition and $\alpha_4 < 0$ for a first-order phase transition.

[6]The whole RAM is however not of ferroelectric nature.

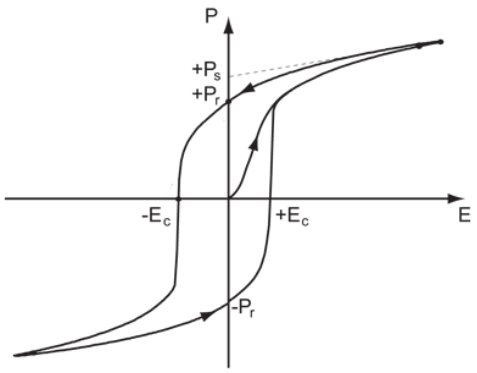

Figure 2.6: Hysteresis loop for a ferroelectric. P_s is the spontaneous polarization, P_r the remanent polarization and E_c the coercive field. One should notice that there is no saturation polarization, as the dielectric properties of the ferroelectric imply that, for $E > E_c$, the total polarization increases with E. For a linear dielectric, the total polarization is then given by $P = P_s + \chi\epsilon_0 E$.

If $\tilde{T}_c$is the critical temperature defined for second-order phase transitions, the ferroelectric critical temperature T_c is determined from the conditions

$$\begin{array}{rcccl} F - F_0 & = & 0 & = & \tilde{\alpha_2}(T - \tilde{T}_c)P^2 + \alpha_4 P^4 + \alpha_6 P^6, \\ \partial F/\partial P & = & 0 & = & 2\tilde{\alpha_2}(T - \tilde{T}_c)P + 4\alpha_4 P^3 + 6\alpha_6 P^5, \end{array} \tag{2.8}$$

from which we have

$$\begin{array}{rcll} T_c & = & \tilde{T}_c + \frac{\alpha_4^2}{4\tilde{\alpha}_2\alpha_6} & \text{(first-order)}, \\ T_c & = & \tilde{T}_c & \text{(second-order)}. \end{array} \tag{2.9}$$

The second-order case is as sketched in figure 2.1 for $\psi = P$, with two stable states for $T < T_c$. Figure 2.7 shows $F - F_0$ vs P in the first-order case, where we can see that there are three stable states for $T = T_c$ and again two for $T < T_t$.

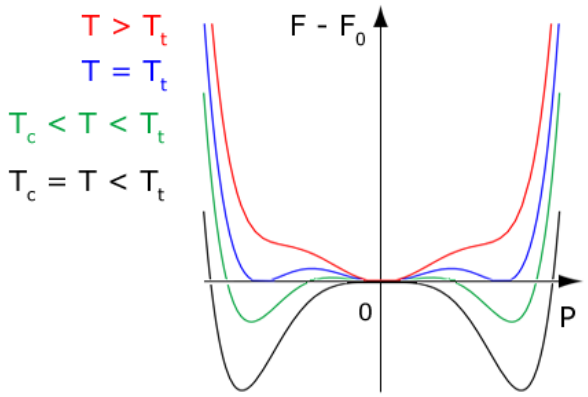

Figure 2.7: Free energy vs. order parameter for first-order phase transitions.

Perovskite structure. Unlike magnetism, ferroelectricity comes from a structural instability. Ferroelectric compounds often present a complex crystal structure, such that of Rochelle

salt. However, one type of material particularly important for our understanding of ferroelectricity are the perovskite oxides, due to their simple crystal structure and the fact that perovskite ferroelectrics usually exhibit a high remanent polarization value. Their chemical formula is ABO_3, with mono- or divalent A atoms at the corners of the unit cell, tetra- or pentavalent B atoms body-centered and the O face-centered, as illustrated in figure 2.8. In addition, this class of materials can present many other instabilities, such as charge, magnetic or superconducting instabilities.

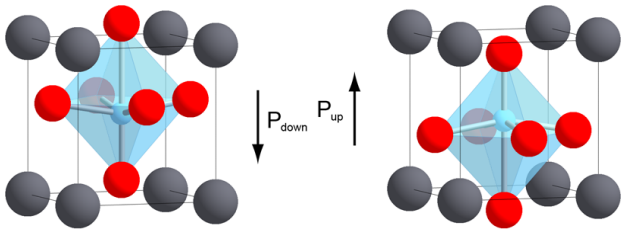

(a) P_{down}. (b) P_{up}.

Figure 2.8: Elementary cell of $PbTiO_3$ in the 'up' and 'down' spontaneous polarization states.

Microscopically, a ferroelectric transition can in general be associated with the freezing of a soft (or low-frequency) phonon mode of lattice motion, usually at the Brillouin zone centre, which generates opposite displacements of positive and negative charge in the unit cell along the polar axis. Ferroelectrics are also often categorized as being of either displacive or order-disorder character, depending whether the paraelectric phase is microscopically non-polar (displacive) or only non-polar in a macroscopic or thermally averaged sense (order-disorder) [4].

Proper and improper ferroelectricity. In the 'proper' ferroelectrics discussed so far, structural instability towards the polar state, associated with the electronic pairing, is the main driving force of the transition. If, on the other hand, polarization is only a part of a more complex lattice distortion or if it appears as a 'side-effect' of some other ordering, the ferroelectricity is called 'improper'. Examples include geometrically induced ferroelectricity due to a structural transition, e.g. in hexagonal manganites $RMnO_3$ (R = Ho-Lu, Y), electronically induced ferroelectricity due to charge ordering ($LuFe_2O_4$) and magnetically induced ferroelectricity due to magnetic ordering.

2.2 Magnetoelectric coupling

In its most general definition, the magnetoelectric (ME) effect denominates the coupling between electric and magnetic fields in matter. In single-phase compounds, it is traditionally described in Landau theory by writing the free energy F of the system in terms of an applied magnetic field $\vec{H}$ and an applied electric field $\vec{E}$ (ref. [8]).

If we drop the terms corresponding to any spontaneous magnetization or polarization by considering a non-ferroic material, F may be written in Einstein summation convention as:

$$\begin{aligned} -F(E,H) &= -F_0 + \frac{1}{2}\epsilon_0\epsilon_{ij}E_iE_j + \frac{1}{2}\mu_0\mu_{ij}H_iH_j + \alpha_{ij}E_iH_j \\ &+ \frac{1}{2}\beta_{ijk}E_iH_jH_k + \frac{1}{2}\gamma_{ijk}H_iE_jE_k + \cdots, \end{aligned} \tag{2.10}$$

The magnetoelectric effect can then be characterized under the form $P_i(H_j)$ and $M_i(E_j)$, which are obtained by differentiating F with respect to E_i or H_i, and then setting E_j or H_j to 0, respectively:

$$P_i(H_j) = -\frac{\partial F}{\partial E_i}\Big|_{E_j=0} = \alpha_{ij}H_j + \frac{\beta_{ijk}}{2}H_jH_k + \cdots \tag{2.11}$$

$$\mu_0 M_i(E_j) = -\frac{\partial F}{\partial H_i}\Big|_{H_j=0} = \alpha_{ij}E_j + \frac{\gamma_{ijk}}{2}E_jE_k + \cdots \tag{2.12}$$

where $\alpha_{ij}(T)$ accounts for the linear magnetoelectric coupling and the third-rank tensors $\beta_{ijk}(T)$ and $\gamma_{ijk}(T)$ represent the quadratic magnetoelectric coefficients.

Thus, from equations 2.11 and 2.12 one can induce a change in the polarization by applying a magnetic field, or conversely in the magnetization by applying an electric field. The technological applications of such coupling between magnetic and electric ordering are detailed in the following section.

2.3 Multiferroism

2.3.1 Definition

By the original definition, a material is said to be multiferroic if it exhibits at least two ferroic properties. Currently, three forms of ferroic order are recognized: ferromagnetism (see 2.1.2), ferroelectricity (see 2.1.3) and ferroelasticity, which is the display of a spontaneous deformation that is stable and can be switched hysteretically by an applied stress. This definition is usually broadened to include the possibility of antiferroic order, such as antiferromagnetism. Moreover, it is currently debated, for symmetry reasons among others, whether an ordered arrangement of magnetic vortices should be included as a fourth form of ferroic order, termed ferrotoroidicity (ref. [13] and [14]).

In a multiferroic material, one expects not only a direct effect of an external field on the corresponding ferroic order, but also the effects of cross-coupling, as represented in figure 2.9. Changes in strain as a function of an electric or magnetic field are shown by the black arrows, and the magnetoelectric coupling between the ferroelectric and ferromagnetic orders is shown by the green arrows.

Ferromagnetic and ferroelectric materials often possess large permeability and permittivity, respectively, which in the Landau formalism described in 2.2 means that a multiferroic that is ferromagnetic and ferroelectric is liable to exhibit large linear magnetoelectric coupling. Indeed, Brown et al. [12] have shown that the linear magnetoelectric coefficient α_{ij} is bounded by the geometric mean of the diagonalized tensors ϵ_{ii} and μ_{jj} such that:

$$\alpha_{ij}^2 \leq \epsilon_0\mu_0\epsilon_{ii}\mu_{jj} \tag{2.13}$$

However, a material does not require a large ϵ_{ij} (μ_{ij}) to be ferroelectric (ferromagnetic). For example, the ferroelectrics KNO_3 and $BaTiO_3$ have dielectric constants $\epsilon = 25$ and $\epsilon = 10'000$ respectively near their Curie temperature of 120 °C. Therefore, large magnetoelectric coupling need not arise in, or be restricted to, multiferroic materials. Figure 2.10 summarizes the classification of insulating oxides after their electric and magnetic properties: ferromagnetic and

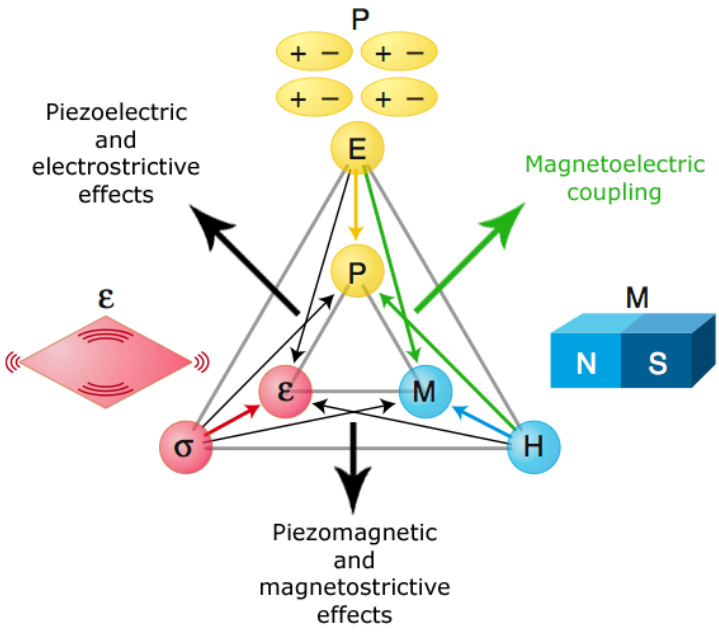

Figure 2.9: Ferroic orders and possible couplings between them, adapted from [7].

ferroelectric materials (thick black and green lines) form subgroups of magnetically and electrically polarizable materials respectively, and their intersection is defined as multiferroic materials (dashed red lines). Magnetoelectric materials (blue dashed lines) are defined as materials in which the magnetoelectric coupling is allowed by symmetry, but may not necessarily be large for one or both types of polarizations. For this reason, there are non ferroic materials that exhibit a large magnetoelectric coupling as well as multiferroic materials that do not exhibit a large magnetoelectric coupling.

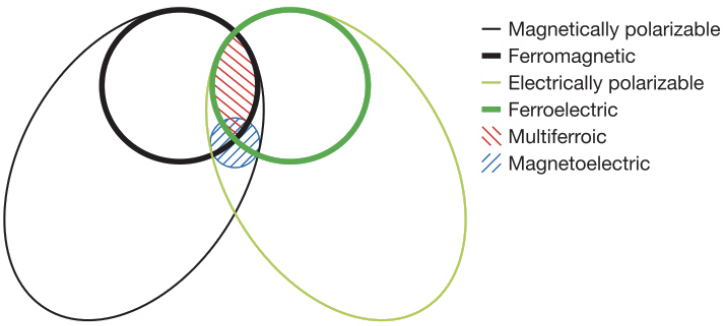

Figure 2.10: Multiferroic and magnetoelectric materials, from [5].

Specific device applications that have been suggested for multiferroic materials include multiple-state memory elements, electric-field controlled ferromagnetic resonance devices and transducers with magnetically modulated piezoelectricity (ref. [9]). In addition, the ability to couple with either the magnetic or the electric polarization offers an extra degree of freedom

in the design of conventional actuators, transducers and storage devices, and a possible way of overcoming the shortcomings or disavantages of current technologies.

However, attempts to design multiferroics that combine ferromagnetism and ferroelectricity in the same phase have proven unexpectedly difficult. The scarcity of these compounds can be understood by examining the required conditions for both ferroic properties to coexist in a single phase.

2.3.2 Coexistence of magnetism and ferroelectricity

Symmetry. Among the 122 Shubnikov crystalline point groups, 13 allow both a spontaneous electric and magnetic polarization; despite this, experimental observation of ferromagnetic ferroelectric materials are even more rare than this ratio would suggest. In fact, many candidate materials that are not multiferroic belong to one of the allowed symmetries.

Electrical properties. By definition, a ferroelectric must be an insulator, whereas ferromagnets, although not required to have specific electrical properties, are often metals. For example, the driving force of ferromagnetism in the elemental ferromagnets Fe, Co and Ni and their alloys is the high density of states at the Fermi level, which also results in metallicity. However, most ferrimagnets and weak ferromagnets are insulators, and there are also very few antiferromagnetic ferroelectrics, even though antiferromagnets are usually insulating materials.

d electrons. The formation of magnetic moments in matter results from partially filled d electron shells. On the other hand, the conventional mechanism for non-centro-symmetry in ferroelectrics, summarized by Hill in [9], formally requires a d^0 electron configuration on the B cation. Hill shows that, although there is a number of factors influencing this requirement, the d electron occupancy of the transition metal is a critical variable in a multiferroic system and is primarily responsible for the scarcity of ferromagnetic ferroelectrics.

Because of the latter condition, a possibility for ferroelectricity and magnetism to coexist in a single-phase material is that the atoms that move off centre to form the electric dipole moment should be different from those that carry the the magnetic moment. However, such materials tend to exhibit only a weak magnetoelectric coupling. A possible alternate route is to search for improper ferroelectricity mechanisms, which put lower constraints on the coexistence with magnetism. In particular, magnetically induced ferroelectricity is especially appealing and is briefly addressed in the following paragraph.

2.3.3 Magnetically driven improper ferroelectricity

As mentioned in section 2.1.3, one particularly promising application of the magnetoelectric effect is the induction of improper ferroelectricity by magnetic ordering, leading to multiferroic compounds. Materials with electric dipoles induced by magnetic ordering present a significant interest for applications, because such dipoles are highly tuneable by applied magnetic fields (ref. [10]). Studies of magnetic tuneability of electric polarization and dielectric constant in some of the orthorhombic rare-earth manganites $RMnO_3$ show an onset of ferroelectricity correlated with the appearance of a spiral magnetic ordering. This is a consequence of magnetic frustration, in which competing interactions between spins preclude simple magnetic ordering.

The mechanism for magnetically induced ferroelectricity and the role of frustration have to

do with the fact that the magnetoelectric coupling is governed by the symmetries of the order parameters $\vec{P}$ and $\vec{M}$. As mentioned in section 2.1.1, $\vec{P}$ is invariant under time reversal, while $\vec{M}$ is invariant under spatial inversion. Therefore, a linear coupling between $(\vec{P}, \vec{E})$ and $(\vec{M}, \vec{H})$ is only possible when they vary in both time and space. The role of magnetic frustration is to induce spatial variations of magnetization, as the magnetic spiral ordering stabilized by the frustration breaks time-reversal and inversion symmetries.

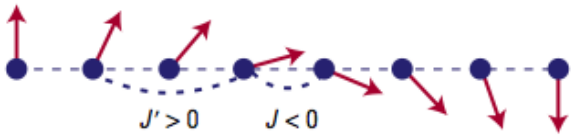

Figure 2.11: Frustrated spin chains with nearest-neighbor ferromagnetic and next-nearest neighbor antiferromagnetic interactions J and J', from [10], in the Heisenberg model $H_H = \sum_n \left[J\vec{S}_n \cdot \vec{S}_{n+1} + J'\vec{S}_n \cdot \vec{S}_{n+2} \right]$. For $J'/|J| < 1/4$, the ground state is a magnetic spiral.

A microscopic mechanism inducing ferroelectricity in magnetic spirals, discussed in [10], involves the antisymmetric Dzyaloshinskii-Moriya (DM) interaction,

$$\vec{D}_{n,n+1} \cdot \vec{S}_n \times \vec{S}_{n+1}, \tag{2.14}$$

where $\vec{D}_{n,n+1}$ is the Dzyaloshinskii vector. The DM interaction is a relativistic correction to the usual superexchange, proportional to the spin-orbit coupling constant, and favors non-collinear spin ordering. It contributes to the induction of ferroelectricity through the fact that

$$\vec{D}_{n,n+1} \propto \lambda \vec{x} \times \vec{r}_{n,n+1}, \tag{2.15}$$

where λ is the spin-orbit coupling constant, $\vec{r}_{n,n+1}$ is a unit vector along the line connecting the n^{th} and $(n+1)^{th}$ magnetic ions, and $\vec{x}$ is the shift of the oxygen ion from this line (see figure 2.12).

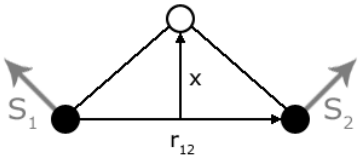

Figure 2.12: Effect of the Dzyaloshinskii-Moriya interaction, adapted from [10]. The Dzyaloshinskii vector depends on the position of the oxygen ion (open circle) between two transition metal ions (filled circles).

Thus, the energy of the DM interaction increases with $\vec{x}$, describing the degree of inversion symmetry breaking at the oxygen site. Because in the spiral state the vector product $\vec{S}_n \times \vec{S}_{n+1}$ has the same sign for all pairs of neighboring spins, the DM interaction pushes negative oxygen ions in one direction perpendicular to the spin chain formed by positive magnetic ions, thus inducing electric polarization perpendicular to the chain. This phenomenon is known as exchange

striction. As spiral states are characterized by the wavevector $\vec{Q}$ and the axis $\vec{e}_3$ around which spins rotate, the induced polarization $\vec{P}$ is then given by (see figure 2.13).

$$\vec{P} \propto \vec{e}_3 \times \vec{Q}. \tag{2.16}$$

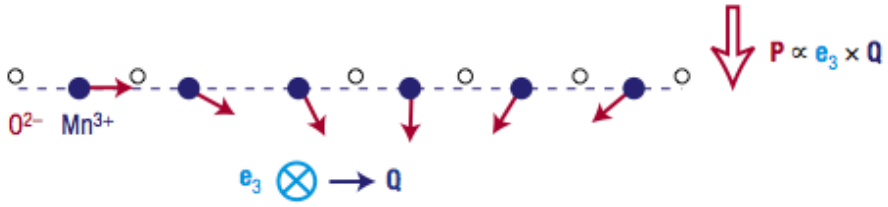

Figure 2.13: Magnetically induced ferroelectricity through the DM interaction in an $RMnO_3$ spin chain, from [10].

This formula (eq. 2.16) for the induced polarization agrees well with many multiferroics. However, the general expression for magnetically induced polarization is more complicated, for instance when the spin rotation axis $\vec{e}_3$ is not oriented along a crystal axis or when the crystal unit cell contains more than one magnetic ion. Furthermore, spiral spin ordering is not the only possible source of magnetically induced ferroelectricity, as pointed out by Cheong and Mostovoy in [10], and other mechanisms than the DM interaction may raise significant interest, as the magnetoelectric coupling in frustrated magnets is shown to be rather weak.

2.4 Two-phase heterostructures

Despite the possible mechanisms for multiferroism, there are significant challenges in finding technologically interesting single-phase compounds. This is principally due to the fact that most of them either lack a large magnetoelectric coupling, or fail to be multiferroic at room-temperature. In particular, magnetic frustration, in addition to contributing to only a weak magnetoelectric coupling, usually delays magnetic transitions down to low temperatures. Furthermore, only two classes of single-phase multiferroics have to this day been successfully prepared as thin films: hexagonal manganites and the Bi-based perovskites. The need for an alternate strategy for engineering enhanced magnetoelectric coupling and room-temperature multiferroics has led to the fabrication and study of articifical composite materials, comprised of a ferroelectric and a magnetic phase with high transition temperature, indirectly coupled via strain.

To this end, efforts to optimize the cross-coupling effects in composite multiferroics with magnetostrictive and piezoelectric materials have led to two main kinds of thin-film architectures: horizontal heterostructures or superlattices, in which heteroepitaxy at the interfaces can be used to control magnetoelectric coupling at the atomic scale, and nanoscale vertical heterostructures, in which coupling occurs through vertical heteroepitaxy (see figure 2.14).

Vertical heterostructures such as the nanopillar geometry illustrated in figure 2.14(b), in which one of the two phases organizes into nanoscale columns embedded in a matrix of the

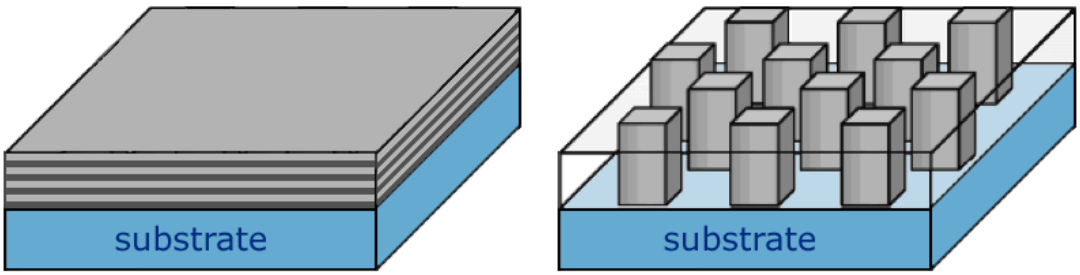

(a) Multilayer (horizontal) heterostructure. (b) Nanopillar (vertical) heterostructure.

Figure 2.14: Schematic representation of examples of horizontal and vertical architectures for two-phase (light and dark gray) multiferroic composites.

other phase, offer a number of advantages over the horizontal heterostructures (ref. [6]). First, they can have a larger interfacial surface area and are intrisically epitaxial in three dimensions, in principle allowing for stronger magnetoelectric coupling. In addition, substrate-imposed mechanical clamping, which is known to suppress both the piezoelectric response and the magnetoelectric coupling due to lattice deformation in thin films, should be reduced in the vertical architecture.

The prototypical multiferroic vertical nanostructure consists of a magnetic spinel phase embedded in the ferroelectric matrix. The first example from Zheng et al. (ref. [15]) was formed of spinel $CoFe_2O_4$ and ferroelectric $BaTiO_3$, and several other combinations of perovskites ($BaTiO_3$, $PbTiO_3$, $BiFeO_3$ and $SrTiO_3$) and spinels ($CoFe_2O_4$, $NiFe_2O_4$ and Fe_3O_4) have since been studied. However, the design and control of such heterostructures remains a challenge.

Morever, much research is still needed to understand the nature of the coupling mechanisms in these composites. In 2005, Zavaliche et al. (ref. [11]) have reported evidence of strong magnetoelectric coupling in $CoFe_2O_4$-$BiFeO_3$ thin films using local probe techniques to show switching of the magnetization in the magnetic $CoFe_2O_4$ phase on reversal of the ferroelectric $BiFeO_3$ phase. The present work focuses on similar studies as an attempt to further characterize the magnetoelectric coupling in the $CoFe_2O_4$-$BiFeO_3$ system.

Chapter 3

The $BiFeO_3$-$CoFe_2O_4$ system

3.1 Structural properties of $BiFeO_3$ and $CoFe_2O_4$

3.1.1 Perovskite structure and ferroelectricity in $BiFeO_3$

$BiFeO_3$ (BFO) has been intensively studied since 1960, due to the coexistence of antiferromagnetic and ferroelectric ordering in the bulk form of this material, with Néel temperature $T_N \sim 643$ K and Curie temperature $T_C \sim 1103$ K. In bulk single crystal form, the material shows a rhombohedrally distorted perovskite structure with space group Rc3, where the oxygen octahedra are displaced along the [111] diagonal, inducing ferroelectric ordering (ref. [16], [18]). These octahedra are rotated along the [111] diagonal alternatively in one direction and the other, so that the real unit cell is rhomboedral and comprises two 'pseudocubic' perovskite unit cells (see figure 3.1).

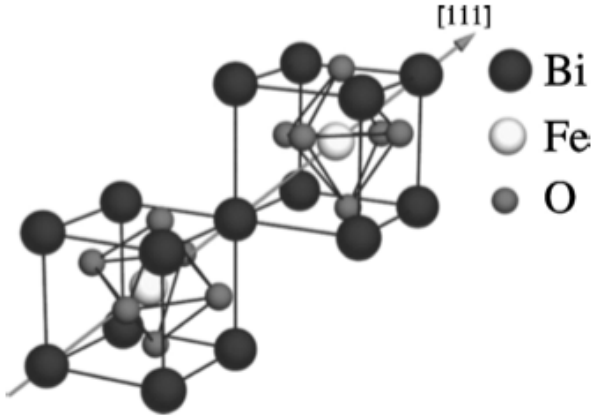

Figure 3.1: Bulk BFO rhombedral unit cell, from ref. [18].

Although initially some spread was observed in the measured ferroelectric polarization values due to varying crystal quality, there is now agreement that these values are some of the highest among ferroelectric materials, with a spontaneous polarization along the [111] direction of 100 $\mu C/cm^2$ measured by Lebeugle et al. (ref. [17]) in 2007 in a BFO single crystal. Epitaxial thin

films exhibit $P_s \sim 60\ \mu C/cm^2$ in the out-of-plane direction. These high polarization values, together with the high T_c and the absence of lead, make BFO an interesting candidate for industrial applications such as FeRAM.

The Fe magnetic moments are ferromagnetically coupled within the (111) planes, with neighboring planes ordering antiferromagnetically, leading to G-type antiferromagnetism in the material as a whole. If the magnetic moments are oriented perpendicular to the [111] direction, the symmetry also permits a canting of the antiferromagnetic sublattices, resulting in Dzyaloshinskii-Moryia type weak ferromagnetism (see section 2.3.3). Figure 3.2 shows the magnetic moment orientations in the ideal and canted G-type antiferromagnetism in BFO. In bulk BFO, an incommensurate spiral spin structure superimposed on the antiferromagnetic ordering leads to a cancellation of the macroscopic magnetization and inhibits the linear magnetoelectric effect. However, large magnetoelectric coupling has been reported in high quality epitaxial thin films.

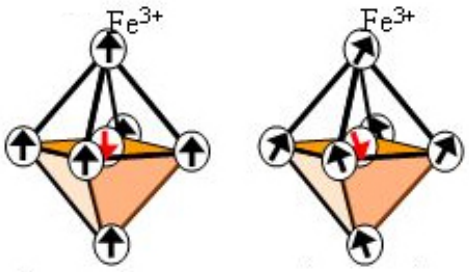

(a) Ideal. (b) Canted.

Figure 3.2: Ideal and canted G-type antiferromagnetism.

In the framework of composite samples, the ferroelectric properties of BFO have led to evidence of strong magnetoelectric coupling in the work of Zavaliche et al., raising a high interest in the $BiFeO_3$-$CoFe_2O_4$ system. However, the mechanism of this coupling is not yet fully understood, and in particular, the role potentially played by the magnetic ordering in the BFO phase remains unclear.

3.1.2 Spinel structure and ferrimagnetism in $CoFe_2O_4$

$CoFe_2O_4$ (CFO) belongs to the spinel family, which is a group of compounds with a chemical formula of AB_2O_4, where A and B can be di-, tri- or tetravalent cations. The standard spinel structure consists of the A atoms occupying all of the tetrahedral coordination sites and the B atoms occupying all of the octahedral sites. CFO has an inverse spinel structure, where the Co cations occupy one half of the octahedral coordination site, half the Fe cations occupy the other half of the octahedral coordination sites, and the other half of Fe cations occupy all the tetrahedral coordination sites. The crystal structure of CFO is shown in figure 3.3.

Spinel structures exhibit ferrimagnetic ordering, originating from the presence of different magnetic moments of the same cation on different sites. The total magnetization can be fairly well predicted by Néel's two-sublattice model, where two internal Weiss fields are assigned to the A and B sublattices, with magnetization M_A and M_B. The internal fields arise from A-A, B-B and A-B superexchange interactions, with the interactions between the same ions assumed

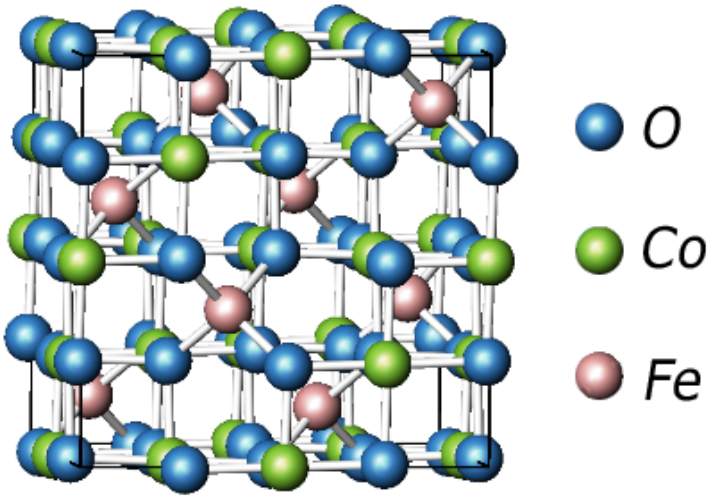

Figure 3.3: Inverse spinel structure in CFO.

to be ferromagnetic and those between different element ions to drive antiparallel alignment. The total magnetization is

$$M = M_A + M_B = \alpha n \mu_A + \beta n \mu_b, \tag{3.1}$$

where n is the number of magnetic ions per unit volume, α and β are the fraction of A and B ions, and μ_A and μ_B are the average magnetic moments of an A and B ion.

3.2 Sample growth

The BFO-CFO nanocomposite thin films studied in this work were grown by N. Dix in the group of J. Fontcuberta in the Institut de Ciència de Materials de Barcelona-CSIC, in the framework of a study of the dependence of the lattice strain of the composite system on growth temperature and different substrate orientations (ref. [19]).

The samples were prepared on Nb(0.5%)-doped $SrTiO_3$ (001) and (111) oriented substrates by pulsed laser deposition. To ensure uniform film composition for a given set of growth conditions, substrates with both crystalline orientations were placed in the growth chamber simultaneously. The two phases organize through self-assembled growth in a nanopillar geometry (see section 2.4). For the adequate range of growth temperature, x-ray diffraction (XRD) θ-2θ measurements show the presence of the perovskite and the spinel phases with out-of-plane cell parameters close to bulk ones. In addition, XRD ϕ scans show that the two phases grow epitaxially with [100]BFO(001)$\|$ [100]STO(001) and [100]CFO(001)$\|$ [100]STO(001). Moreover, no spurious phases are observed in those films. XRD θ-2θ scans for an optimized growth temperature of 650 °C are reported in figure 3.4.

The subtrate orientation plays a drastic role in determining the microstructure of the films, as shown by field emission scanning electron microscopy (FESEM) measurements: whereas nanopillars of CFO in a BFO matrix are formed on (001)STO, nanopillars of BFO in a CFO matrix are formed on (111)STO, and subsequently different interfaces are formed.

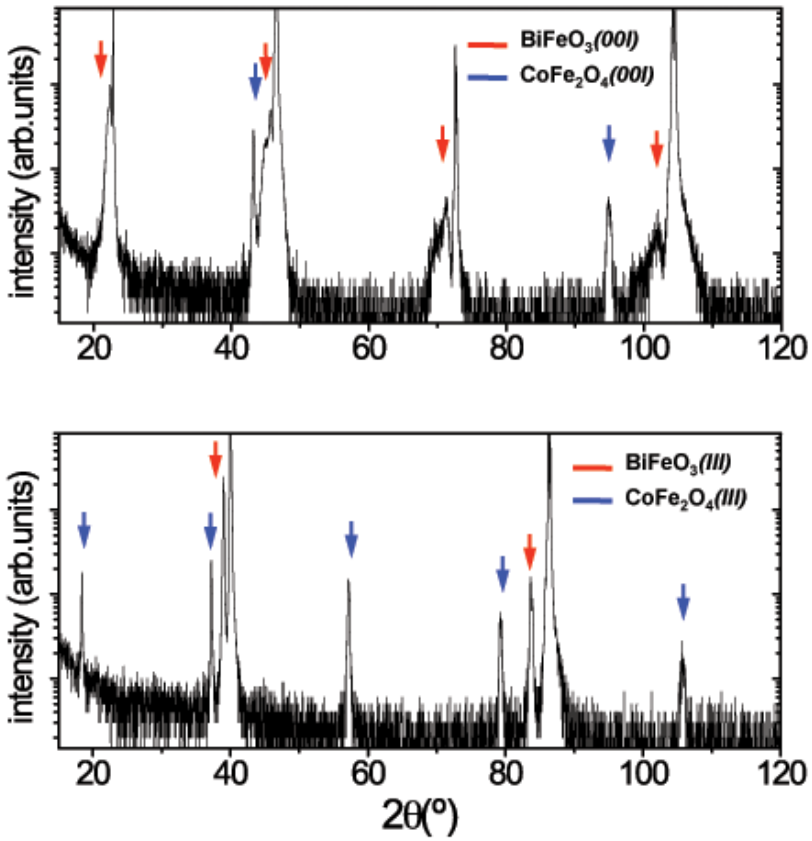

Figure 3.4: XRD $\theta - 2\theta$ measurements on (001) and (111) oriented substrate samples.

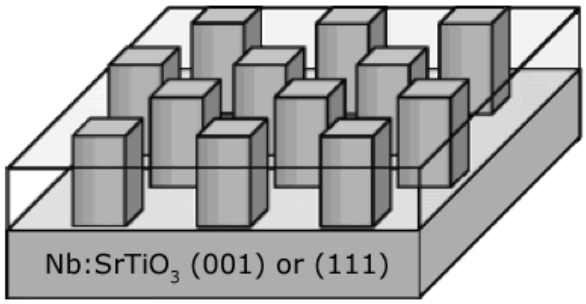

Figure 3.5: Schematic view of the CFO-BFO thin films. The nanopillars correspond to either CFO or BFO, depending on the orientation ((001) vs. (111)) of the substrate.

In addtion, surface energy properties lead to nanopillar faceting, observed by FESEM (see figure 3.7): depending on the substrate orientation, a rectangular geometry for (001) and a triangular geometry for (111) substrate oriented samples are observed.

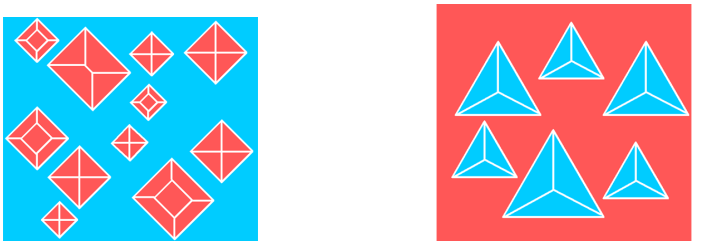

(a) (001) substrate sample. (b) (111) substrate sample.

Figure 3.6: Schematic illustration of the nanopillars facetting in (001) and (111) oriented substrate samples.

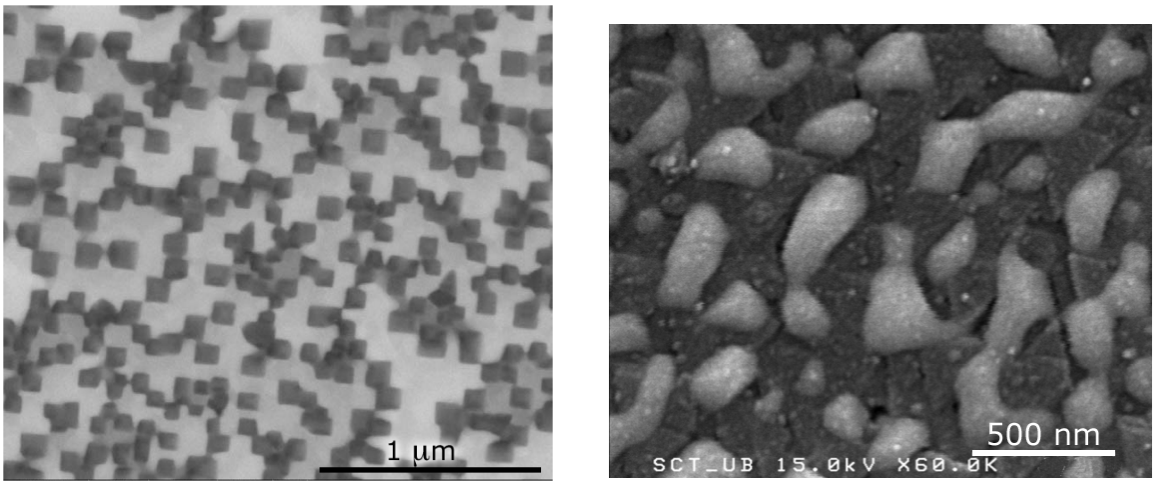

(a) (001) substrate sample. (b) (111) substrate sample.

Figure 3.7: FESEM measurements on (001) and (111) oriented substrate samples using backscattered electrons, showing rectangular and triangular nanopillar faceting, respectively.

Chapter 4

Experimental techniques

4.1 Atomic Force Microscope

The atomic force microscope (AFM) is a type of scanning probe microscope, and one of the foremost tools for imaging, measuring and manipulating matter at the nanoscale. It consists of a microscale cantilever with an atomically sharp tip (probe) on its end that is used to scan over the specimen surface. When the tip is brought close enough to the surface, Coulomb repulsive forces lead to a deflection of the cantilever according to Hooke's law, which can be detected by a laser spot reflecting from the cantilever onto an array of photodiodes, and the tip is said to be in contact.

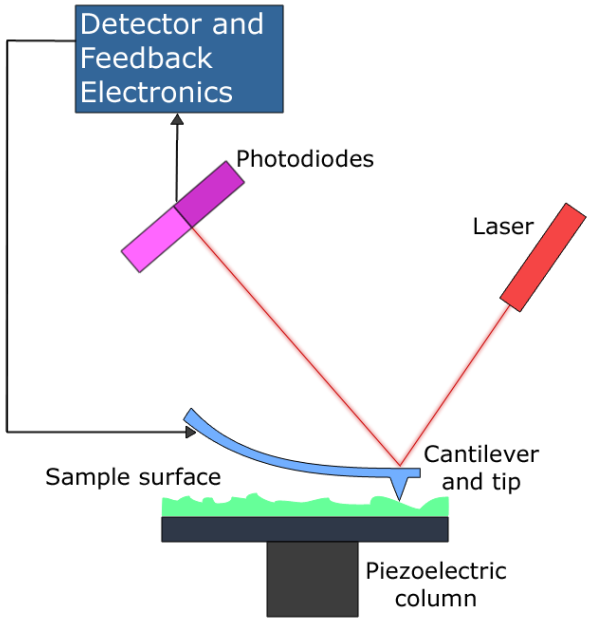

Figure 4.1: Schematic view of an AFM setup.

To maintain a constant tip-to-sample distance, a feedback loop is implemented between the

photodetector and the cantilever. In the AFM model used in this work, a *Digital Instruments Nanoscope MultiMode IV*, the cantilever is maintained fixed in a tip holder, and the sample placed on top of a piezoelectric column that can move in the z direction for height adjusting and in the x,y directions for surface scanning. There are two scanning modes, among others, that can be used for different purposes:

- *Contact Mode* : as described above, the force between the tip and the sample is kept constant by the feedback loop by maintaining a constant cantilever deflection.

- *Resonance Mode* : the cantilever is driven to oscillate near its resonance frequency by a small piezoelectric element mounted in the tip holder; the oscillation amplitude is modified as a result of tip-sample forces, so that the reflected laser beam is deflected in a regular pattern over the photodiode array, generating a sinusoidal electronic signal which is modified by the oscillation amplitude variation. Depending on the height of the tip above the sample, different forces such as electrostatic interaction, magnetic forces, van der Waals attraction, water adhesion and Coulomb repulsion can play a role. If the cantilever enter intermittently into contact with the surface, the technique is known as *tapping mode*; otherwise, it is referred to as *non-contact mode*.

4.1.1 Local application of an electric field

If the AFM tip is made of or coating with a metallic material, a local electric field can be applied through the sample by using a bottom electrode such as a conductive substrate and the AFM tip (usually in contact mode) as a top electrode. In a ferroelectric sample, if the applied electric field is greater than the coercive field, one can then perform local switching of the electric polarization, or 'writing'. Experimental observations show that in fact, the minimal electric field required to switch the polarization is often greater than the coercive field experimentally measured in a simple plane capacitor geometry. This happens principally because of dielectric mismatch leading to a potential drop across an effective dielectric gap, the possibility of tip-sample interactions decreasing the quality of the contact, and because the tip geometry does not produce a homogeneous electric field. Figure 4.2 illustrates the ferroelectric domain switching by using a gate top electrode or by using a conductive AFM tip as a top electrode.

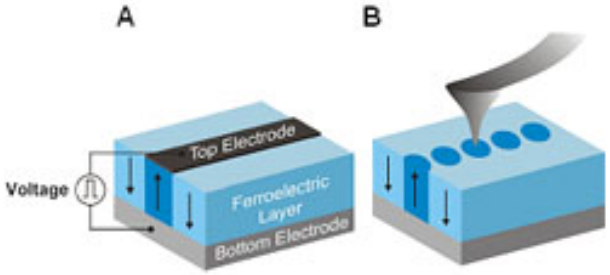

Figure 4.2: Traditional vs. scanning probe techniques to switch ferroelectric domains. The voltage is applied with a gate top electrode or with the metalic tip of an AFM respectively.

4.1.2 Piezoresponse Force Microscopy

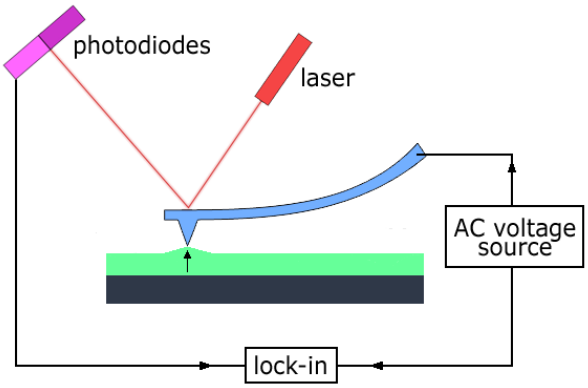

Figure 4.3: Schematic view of PFM imaging.

The local state of the electric polarization can be measured with the AFM in contact mode by the means of Piezoresponse Force Microscopy (PFM), that exploits the piezoelectric behavior of the sample material. An AC voltage with lower amplitude than the writing voltage is applied through the sample between the tip and the bottom electrode, inducing a local modulation in the piezoelectric layer thickness. Depending on the orientation of the electric dipoles, i.e. parallel or anti-parallel to the applied field, the resulting oscillating deformation will be in phase or out-of-phase by π with respect to the input signal. This output signal then provides information about the local state of polarization, with its phase being related to the sign of the polarization and its amplitude to the deformation amplitude.

A PFM signal image of the out-of-plane polarization can therefore be recorded from the vertical movements of the AFM tip. Similarly, the lateral movements of the tip may be be recorded to construct a map of the in-plane polarization (perpendicular to the length axis of the cantilever) of the scanned region.

4.1.3 Magnetic Force Imaging

Magnetic Force Microscopy (MFM) allows the local mapping of the spatial distribution of magnetism at the nanoscale, by measuring the magnetic interaction between the sample and the AFM tip. To this end, a magnetically coated tip is used, and the deflection due to magnetic interaction is separated from topographic contribution by using *interleave scanning*.

In interleave scanning mode, two passes in tapping mode are made over each scan line. The first one records topographic information, that is then used during the second pass, where the feedback is turned off and the tip is lifted to a user-selected height above the surface, to keep the tip at a constant distance from the surface. The influence of magnetic or electrostatic forces is then measured using the principle of force gradient detection, which states that the cantilever resonant frequency f_0 is shifted by an amount Δf proportional to vertical gradients in the magnetic or electrostatic forces on the tip. Usually, Δf tends to be very small with respect to f_0, typically in the 1-50 Hz range for cantilevers with a resonant frequency $f_0 \sim 100$ kHz, and can be detected through various ways. In this work, phase detection, which measures the cantilever oscillation phase relative to the piezoelectric drive, was used.

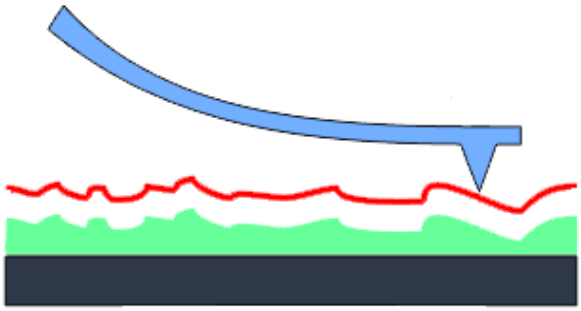

Figure 4.4: Schematic view of interleave scanning mode, with the red path indicating the second scan pass above the surface.

4.2 Scanning Electron Microscope

The Scanning Electron Microscope (SEM) is a type of electron microscope that images the sample surface by scanning it with a high-energy beam of electrons. The electrons are thermionically emitted from a tungsten filament cathode and accelerated towards an anode, with a typical energy ranging from a few hundred eV to 40 keV. One or two condenser lenses focus the beam to a very fine focal spot from 0.4 nm to 5 nm radius, and pairs of scanning coils deflect the beam horizontally and vertically so that it scans in a raster fashion over a rectangular area of the sample surface. When the primary electron beam interacts with the sample, the electrons lose energy by repeated scattering and absorption within a pear-shaped volume of the specimen known as the interaction volume, which extends from less than 100 nm to around 5 μm into the surface.

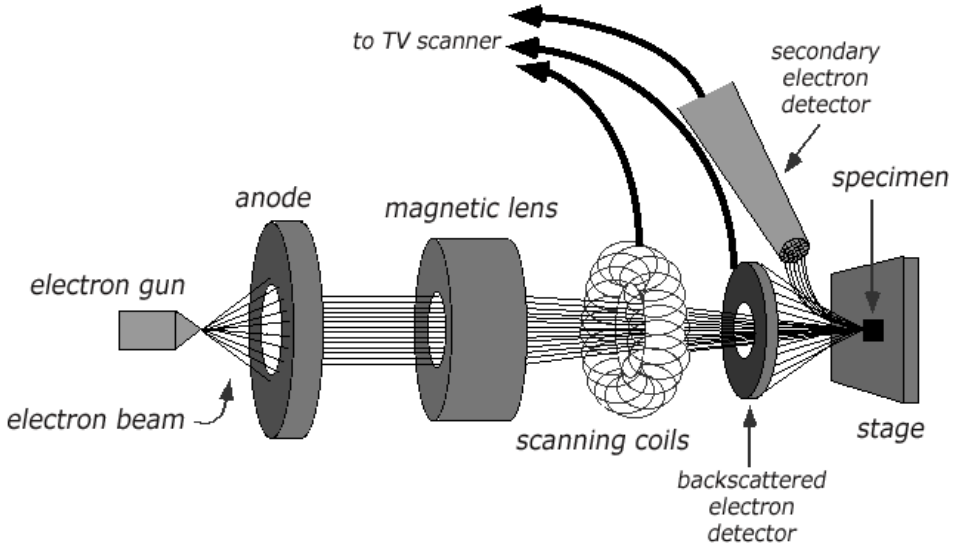

Figure 4.5: Schematic illustration of a SEM (rotated by 90° counter-clockwise).

Imaging can be achieved through the detection of low energy (< 50 eV) secondary electrons, or backscattered electrons. The latter consist of high-energy electrons originating in the electron

beam, that are reflected or back-scattered out of the specimen interaction volume. Backscattered electron imaging is useful for distinguishing one material from another, since the yield of the collected backscattered electrons increases monotonically with the specimen's atomic number. Backscatter imaging can distinguish elements with atomic number differences of at least three, i.e., materials with atomic number differences of at least three would appear with good contrast on the image. Because these electrons are emitted from a depth in the sample, the resolution in the image is not as good as for secondary electrons, with a beam resolution ranging from 10 to 20 nm.

4.3 Superconducting Quantum Interference Device

A Superconducting Quantum Interference Device (SQUID) is very sensitive magnetometer that consists of two superconductors separated by thin insulating layers to form two parallel Josephson junctions. The great sensitivity of the SQUID devices is due to the Josephson effect, allowing changes in magnetic field associated with one flux quantum to be measured. One of the discoveries associated with Josephson junctions was that the flux is quantized in units:

$$\Phi_0 = \frac{2\pi\hbar}{2e} \approx 2.0678 \cdot 10^{-15}\ Tm^2 \tag{4.1}$$

If a constant biasing current is maintained in the SQUID device, the measured voltage oscillates with the changes in phase at the two junctions, which depends upon the change in the magnetic flux, as illustrated in figure 4.6. Detecting this circulating current enables the use of the SQUID as a magnetometer.

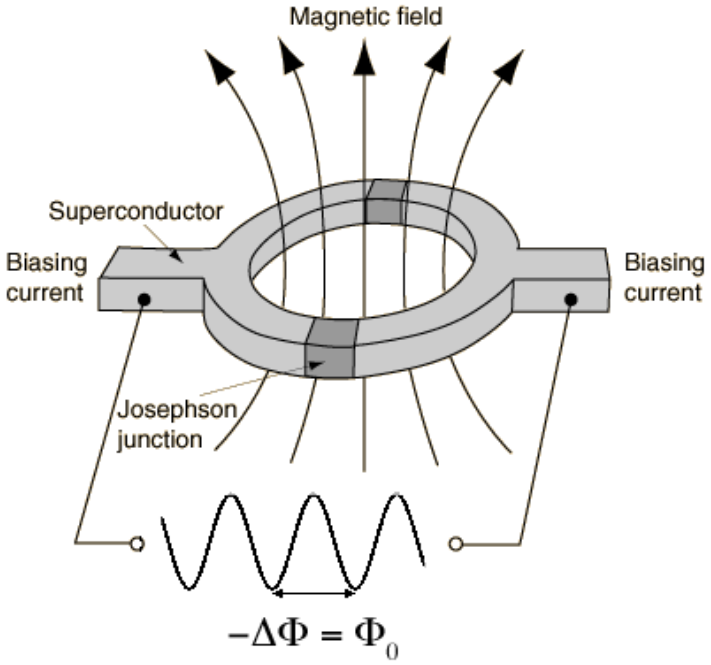

Figure 4.6: Schematic illustration of a SQUID magnetometer: for steadily increasing magnetic flux, one period of voltage variation corresponds to an increase of one flux quantum.

Chapter 5

Results and discussion

5.1 Surface topography characterization

In preparation for subsequent PFM and MFM measurements, surface characterization measurements were initially performed on (001) and (111) oriented substrate samples. These include morphology and roughness investigations, which are paralleled to the results from the group of J. Fontcuberta.

5.1.1 Atomic Force Microscope

An AFM topography scan of a 2×2 μm^2 region on a (001) substrate sample is shown in figure 5.1(a), with a root mean square (rms) roughness of 17 nm. The CFO nanopillars show rectangular faceting, as shown by FESEM measurements from the group of J. Fontcuberta, and a lateral cut analysis (figure 5.1(b)) shows them to have a mean width of 93 nm with a standard deviation of 26 nm. The BFO matrix organizes in flat plateaus (details about the growth conditions influence on the samples morphology can be found in ref. [19]). As the nominal thickness for this sample was measured to be 100 nm, one can appreciate the surface roughness in a three-dimensional view extrapolated from figure 5.1(a), shown in figure 5.2.

Figure 5.3 shows an AFM topography of a 5×5 μm^2 region on a (111) substrate sample. The BFO nanopillars exhibit triangular faceting, again confirmed by FESEM measurements, and have a mean width of 223 nm with a standard deviation of 39 nm. The CFO matrix organizes in faceted prisms, which in turn yields a higher rms roughness of 22 nm.

Both (001) and (111) oriented substrate samples therefore exhibit a columnar nanostructure in agreement with the TEM measurements from the group of J. Fontcuberta, along with a high rms roughness ~ 20 nm with respect to their nominal thickness. From a technological point of view, such a high surface roughness makes PFM and MFM more challenging, as the quality of the contact may not be optimal, or as the tip coating could wear off.

Furthermore, surface aggregates ~ 1 μm wide, as shown in figure 5.4, are observed to uniformly cover both kinds of samples. Because the XRD $\theta - 2\theta$ scans for both kinds show no presence of any spurious phases, SEM measurements were performed on a (001) oriented substrate sample to conduct an elemental analysis on these surface aggregates.

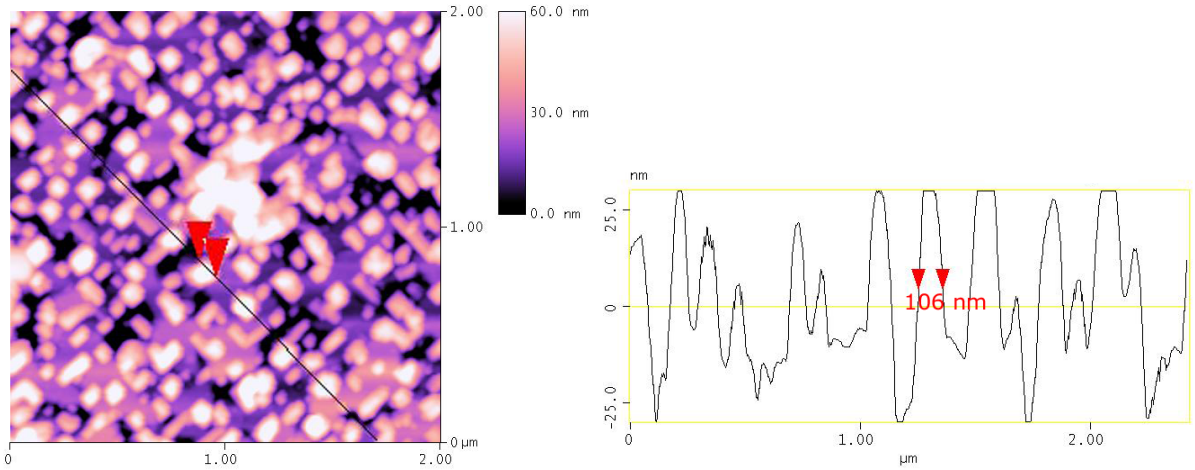

(a) Top view.

(b) Lateral profile along the black line in figure 5.1(a).

Figure 5.1: AFM topography on an (001) oriented substrate sample, showing rectangular faceting of the CFO nanopillars.

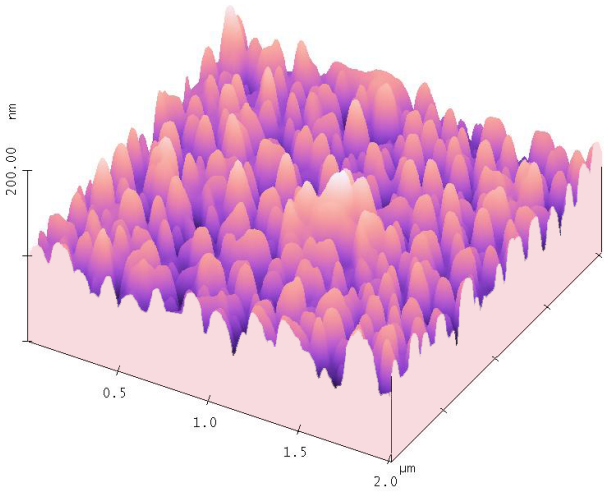

Figure 5.2: Three-dimensional view extrapolated from 5.1(a).

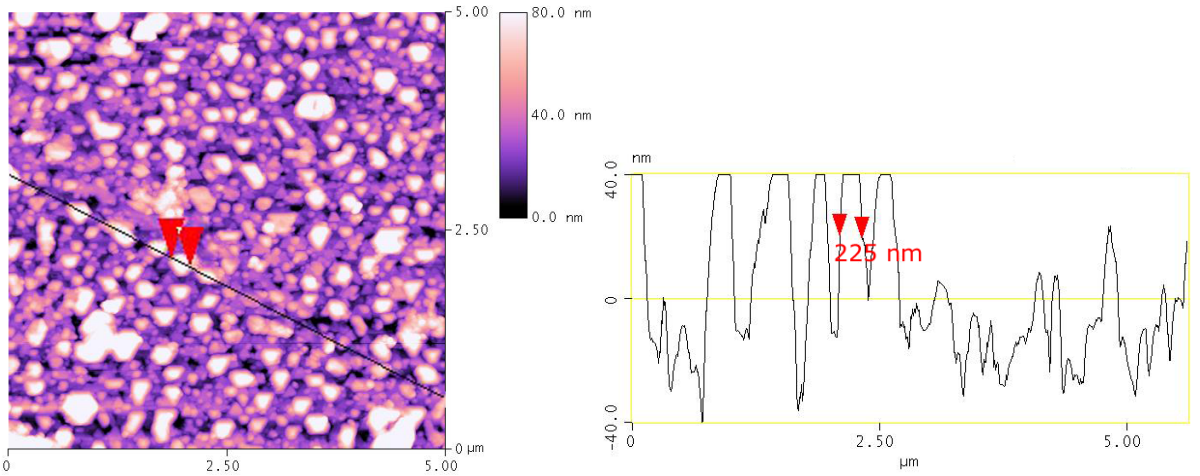

(a) Top view.

(b) Lateral profile along the black line in figure 5.3(a).

Figure 5.3: AFM topography on an (111) oriented substrate sample, showing triangular faceting of the BFO nanopillars.

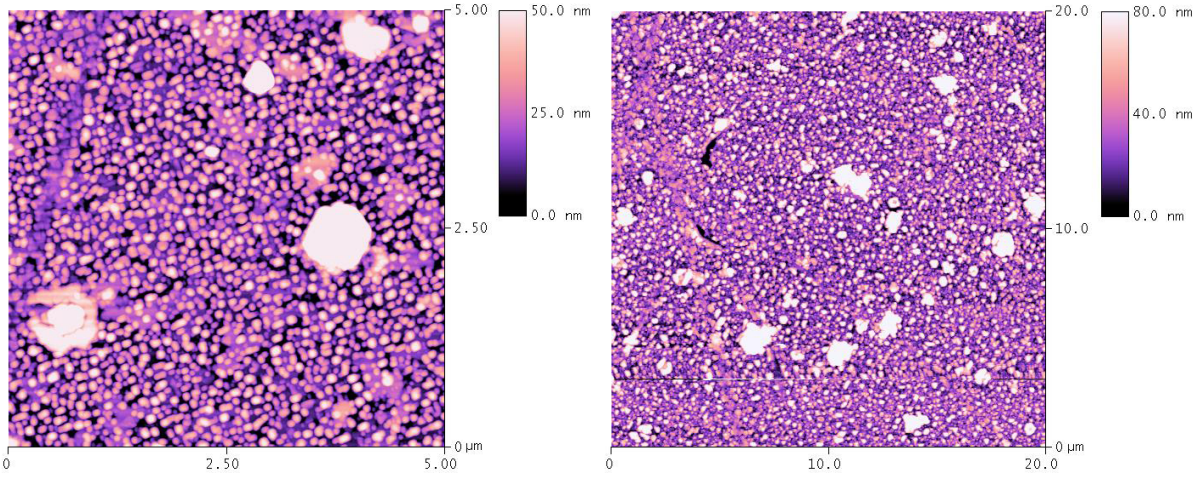

(a) (001) oriented substrate sample.

(b) (111) oriented substrate sample.

Figure 5.4: AFM topography on (001) and (111) oriented substrate sample, showing large surface aggregates.

5.1.2 Scanning Electron Microscope

In order to investigate the chemical composition of the surface aggregates shown by AFM topography, SEM measurements were performed on a (001) oriented substrate sample, using backscattered electron acquired elemental analysis. Figure 5.5(a) shows a 70'000x magnified imaging of the sample surface using backscattered electrons. The surface aggregates can be seen, while the resolution of the SEM beam does not allow to separate the matrix and the nanopillars.

Three spots, indicated by colored marked dots on figure 5.5(a) have been chosen for elemental analysis: one on the largest aggregate in the region (n°1), another on an average aggregate (n°2) and a reference point in a region free from surface aggregates (n°3). Given the resolution of the SEM beam, this third spot includes both the BFO matrix and the CFO nanopillars, and is therefore assumed to reflect the growth target elemental composition. Figures 5.5(b), 5.5(c) and 5.5(d) show the data corresponding to the elemental analysis of the aggregates, with the red curve corresponding to the aggregate free region composition. For the different aggregates examined, as shown in figures 5.5(b) and 5.5(c), a decrease of the Ti signal with respect to the aggregate free region is observed, which comes from the fact that the interaction volume penetrates less deeply into the STO substrate. Both aggregates show a higher presence of Fe, especially noticeable in spot n° 1. Individually, the aggregate measurement in spot n°1 shows a significantly higher Co signature, while that measured in spot n°2 shows an excess of Bi with respect to the expected sample composition.

From these composition analysis, one may therefore expect these large surface aggregates to exhibit either magnetic or ferroelectric behavior.

5.2 Magnetic characterization

In preparation for measurements conducted to probe a possible magnetoelectric coupling in our samples, magnetic and ferroelectric characterization of the CFO and the BFO phase respectively were then performed on (001) and (111) oriented substrate samples.

5.2.1 Superconducting Quantum Interference Device

To obtain a macroscopic magnetic characterization of both kinds of sample, out-of-plane magnetization vs. external magnetic field measurements were performed with a SQUID magnetometer, shown in figure 5.6.

A hysteresis loop with a coercive field of 0.2 T was measured for both samples with different substrate orientations. Remanent magnetization M_{rem} values were measured to be $\approx 60\%$ of the saturation magnetization M_{sat} for the (001) oriented substrate sample, and $M_{rem} \approx 44\%\ M_{sat}$ for the (111) oriented substrate sample. Moreover, relaxations measurements for both kinds of sample over five hours showed no significant decay of the magnetization over time.

While no similar in-plane measurements have been performed, measurements from J. Fontcuberta's group show that the combination of nanopillar shape and heteroepitaxial stresses imposed by the epitaxial matrix yield a perpendicular magnetic anisotropy, so that the easy axis can be considered out-of-plane.

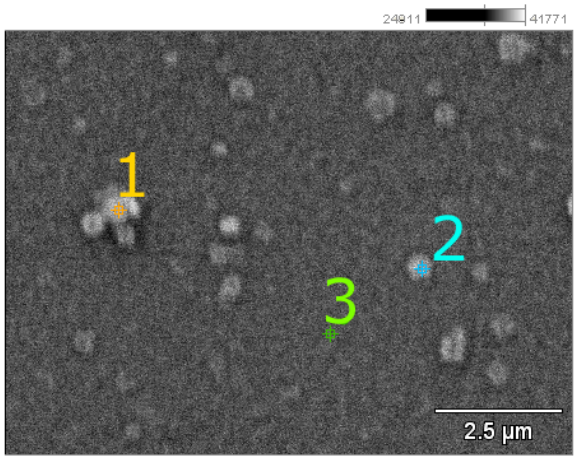

(a) SEM imaging of (001) substrate sample using BSE, showing surface aggregates.

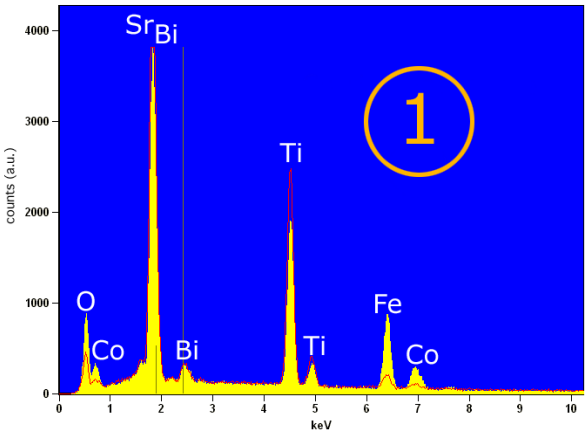

(b) Elemental analysis from spot n°1 in figure 5.5(a), showing Fe and Co excess.

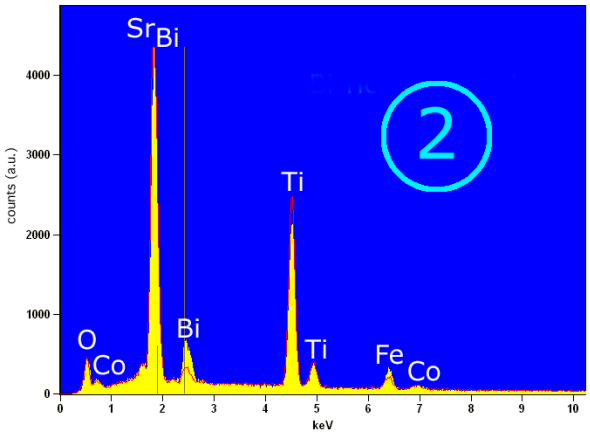

(c) Elemental analysis from spot n°2 in figure 5.5(a), showing Fe and Bi excess.

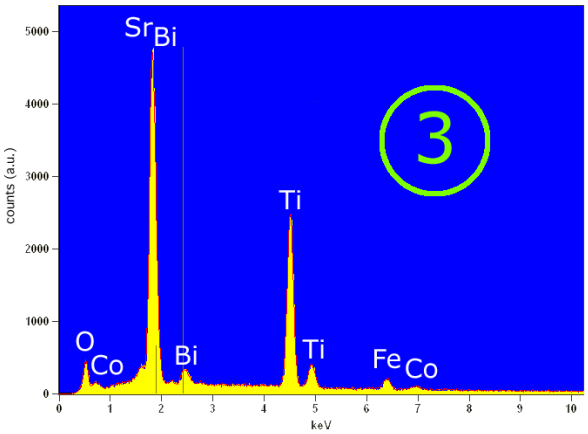

(d) Elemental analysis from spot n°3 in figure 5.5(a), which is assumed to be equal to the growth target composition.

Figure 5.5: SEM elemental analysis on a (001) oriented substrate sample. Surface aggregates measured in spots n° 1 and 2 (in orange and blue respectively in figure 5.5(a)) show an excess of Co and Bi respectively with respect to the assumed growth target composition measured in spot n°3.

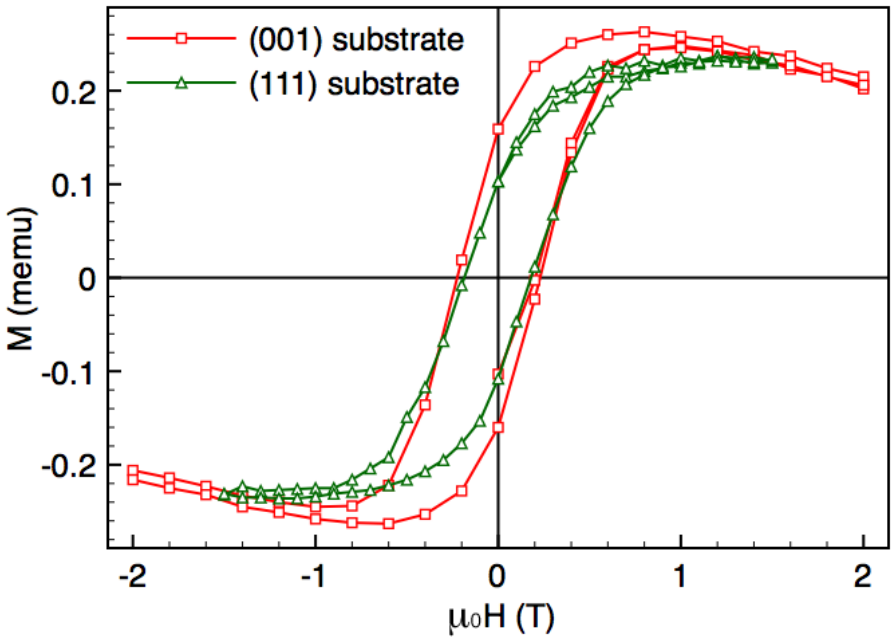

Figure 5.6: Magnetization vs. applied magnetic field SQUID measurements. The negative slope in the red measurement for $|\mu_0 H| > 0.5$ T originates from the diamagnetic contribution of the sample substrate; the green measurment has been stopped before this contribution became visible.

5.2.2 Magnetic Force Microscopy

In order to identify magnetic domains and correlate them with either CFO nanopillars or matrix, local magnetic characterization was performed through MFM measurements. The samples were previously magnetized under 2T magnetic fields. To clearly identify regions with a magnetic signature, MFM scans were carried out twice in each region, with the tip magnetized in opposite directions (upwards and downwards) during the two measurements. With the tip magnetization in the up direction, the up-magnetized domains in CFO appear black on the MFM image (attractive interaction) and the down-magnetized domains appear white (repulsive interaction). The converse is true with the tip magnetization in the down direction. As a result, the two scans of a same region can be substracted to obtain a map of the magnetic domains, regardless of their orientation.

Figure 5.7 shows such a set of MFM measurements over a 5×5 μm^2 region on a (001) oriented substrate sample. On figures 5.7(a) and 5.7(b)(up-magnetized tip), a correlation between magnetic domains and CFO nanopillars is highlighted by green circles. Our measurements suggest that the ferrimagnetic nanopillars are predominantly in a single domain state, which can be correlated to the fact that the average lateral nanopillar size is smaller than twice the critical size for single domain in CFO, which is ~ 70 nm (ref. [20]).

Figure 5.7(c) shows the MFM phase image of the same region with the tip magnetization downwards, and figure 5.7(d) shows the absolute value of the difference between 5.7(b) and 5.7(c), with the contrasting (i.e. magnetic) regions appearing white and the non-contrasting regions appearing black. By using this map of magnetic domains as a support, a statistical

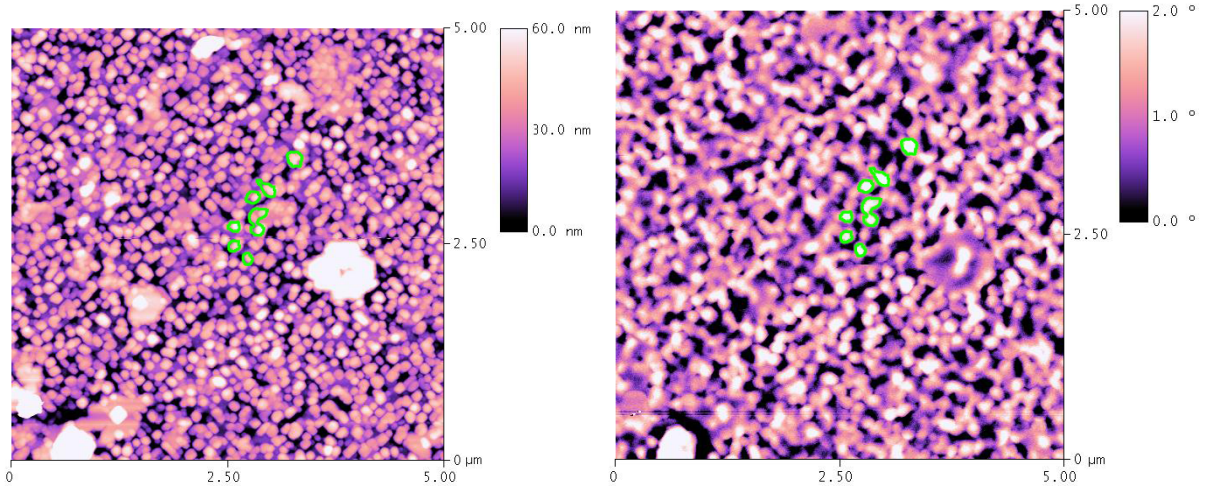

(a) Topography.

(b) Phase, tip magnetization upwards.

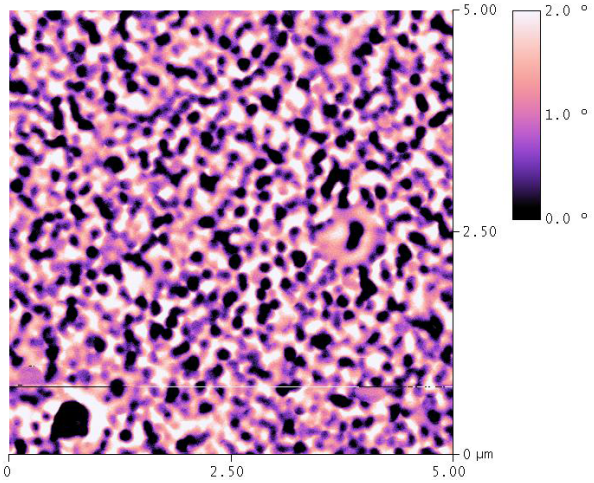

(c) Phase, tip magnetization downwards.

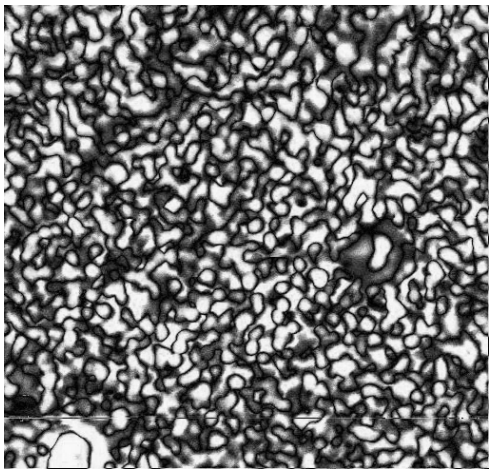

(d) Difference between 5.7(b) and 5.7(c) (arbitrary units).

Figure 5.7: MFM measurements on a (001) oriented substrate sample. Green circles in fig. 5.7(a) and 5.7(b) highlight the correlation between CFO nanopillars and magnetic single domains, suggesting that the nanopillars are preferentially in a single-domain state. The bitmap difference between the MFM with the upwards (fig. 5.7(b)) and downwards (fig. 5.7(c)) tip magnetizations (fig. 5.7(d)) shows magnetic (white) and non-magnetic (black) regions.

analysis over the total number of ferrimagnetic nanopillars yields a ratio of nanopillars magnetized in the preferential (down) magnetization of 79%, visible in figures 5.7(b) and 5.7(c). This result can be correlated to the remanent magnetization value measured by SQUID: with all domains magnetized in the same direction corresponding to M_{sat}, an 80% ratio of preferential magnetization corresponds to $3/5M_{sat} = 80\%M_{sat} = M_{rem}$ (cf. figure 5.8).

Figure 5.8: Schematic illustration of the correlation between the ratio of preferentially magnetized nanopillars and the total remanent magnetization: a 80% ratio of columns magnetized in the preferred direction yields a total magnetization of $3/5 = 60\%$ of the saturation magnetization (where pairs of opposite magnetization columns cancel each other).

Figure 5.9 shows a similar set of MFM measurements over a $10 \times 10\ \mu m^2$ region on a (111) oriented substrate sample. Green contours in figures 5.9(a) and 5.9(d) show a correlation between magnetic domains and inter-pillar (i.e. CFO matrix) regions. Once again, we observe two magnetization orientations, with a proportion of 72% of preferred orientation over the total number of domains. This is again in agreement with the macroscopic SQUID measurements of the magnetization, with a remanent magnetization $M_{rem} \approx 45\%\ M_{sat}$.

As can be seen from figures 5.7 and 5.9, some of the surface aggregates discussed previously exhibit magnetized regions, which agrees with the fact, shown by SEM elemental analysis, that some of them are CFO precipitates.

5.3 Piezoelectric Force Microscopy

The polarization stability and switchability of the BFO in (001) and (111) oriented substrate samples was probed through PFM measurements after electrical poling. An array of alternate stripe domains was written with +12 and -12 V, then imaged using PFM. Images were typically taken over a 14 hour period after poling to eliminate the possible contribution due to surface charging effects, and to confirm polarization stability in the artificially poled domain structure.

Figure 5.10 shows PFM measurements on a (001) oriented substrate sample, where ferroelectric BFO forms the matrix in which the ferrimagnetic CFO nanopillars are embedded. The samples show a good out-of-plane contrast, in spite of the significant surface roughness, and therefore a less-than-optimal tip-surface interaction. Without any previous electrical poling (figure 5.10(b)), the BFO matrix exhibits a polydomain state, with a statistically equivalent proportion of up and down polarization domains. Figure 5.10(c) shows that after poling with five 300 nm wide alternate stripes of +12V (white) and -12V (black), the polarized regions appear fully switched and stable after the 24 hours waiting time.

A similar set of measurements on a (111) oriented substrate sample is shown on figure 5.11, where ferroelectric BFO forms nanopillars embedded in the ferrimagnetic CFO matrix. The out-of-plane contrast is again good, with a tip-sample interaction better than expected due to the even higher surface roughness. Without any previous electrical poling (figure 5.11(a)), the BFO columns show an individual monodomain state; moreover, there is a clear preferential

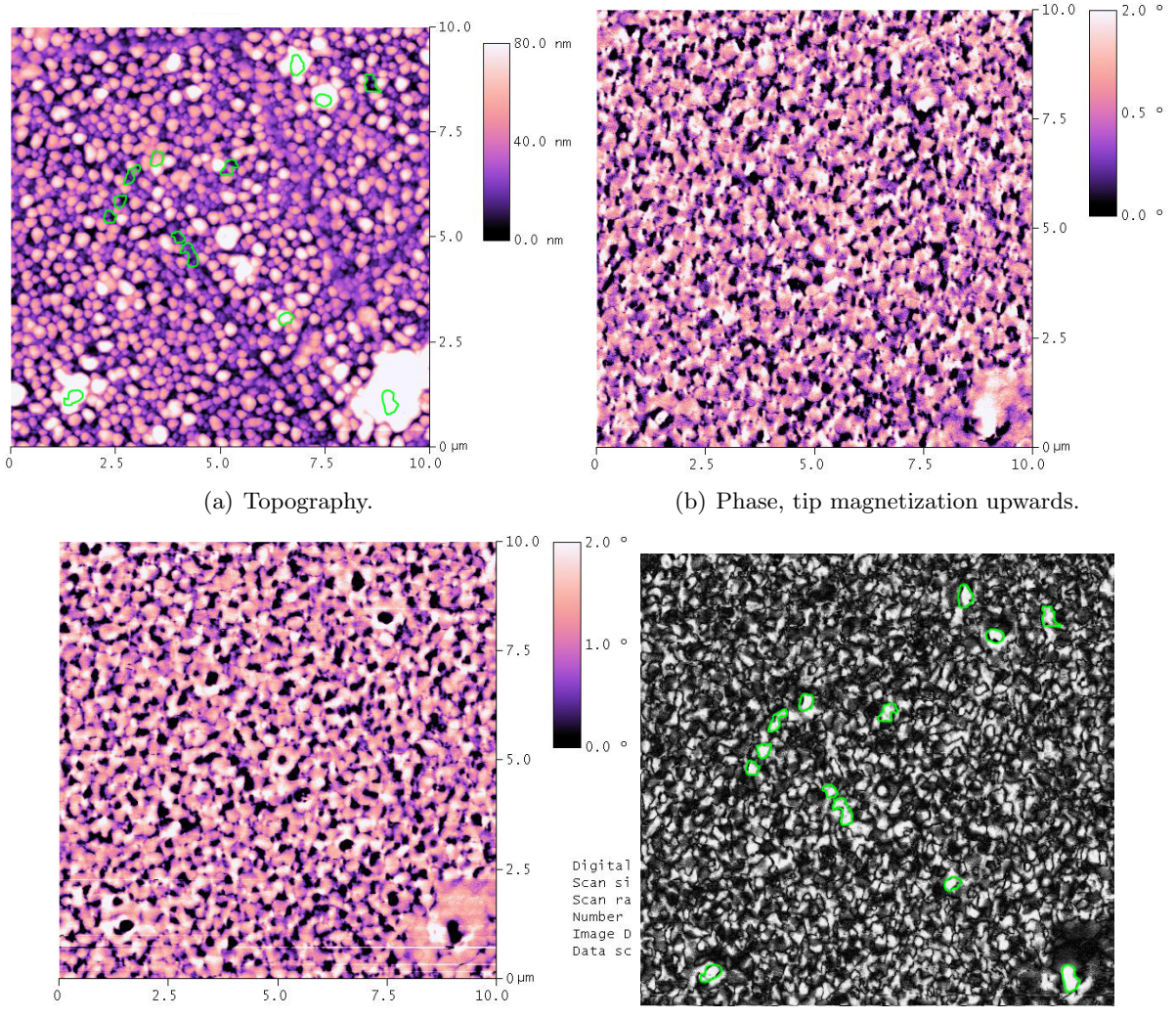

(a) Topography.

(b) Phase, tip magnetization upwards.

(c) Phase, tip magnetization downwards.

(d) Difference between 5.9(b) and 5.9(c).

Figure 5.9: MFM measurements on a (111) oriented substrate sample. The bitmap difference in (d) between the MFM with the upwards (b) and downwards (c) tip magnetizations shows magnetic (white) and non-magnetic (black) regions. Green contours in the topography (a) and the difference image show a correlation between magnetic domains and the CFO matrix.

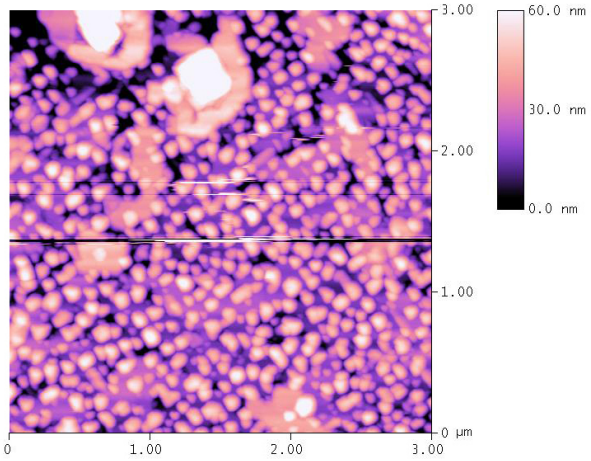

(a) Topography.

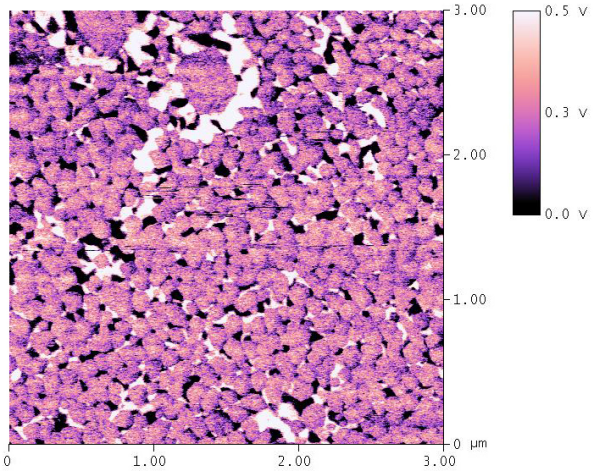

(b) Piezoresponse without any previous poling.

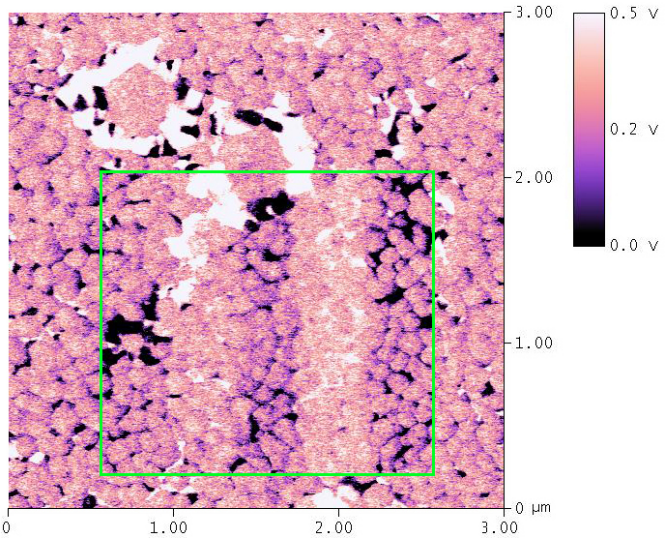

(c) Piezoresponse after poling with five alternate bands of +12 (white) and -12V (black).

Figure 5.10: PFM measurements on a (001) oriented substrate sample. (a) and (b) show the correlation between the topography and the PFM response, without any artificial poling: the BFO matrix offers good out-of-plane contrast and shows a non-preferential polydomain state. (c) shows the PFM image after poling with 300 nm wide stripe domains, which appear fully switched and stable after 24 hours.

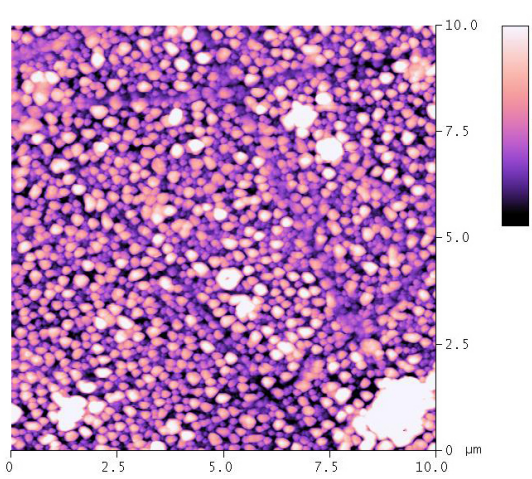

(a) Topography.

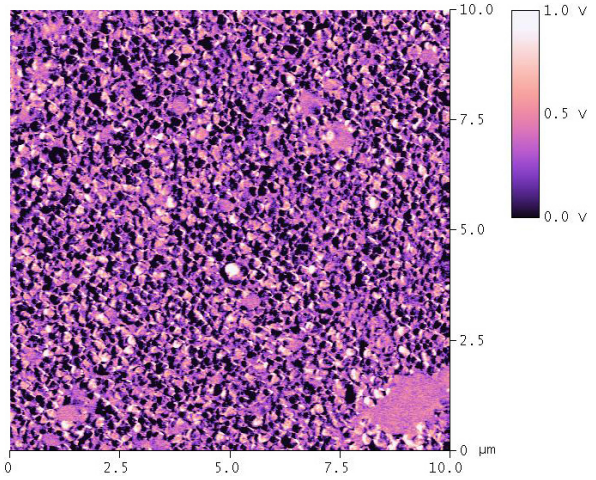

(b) Piezoresponse without any previous poling.

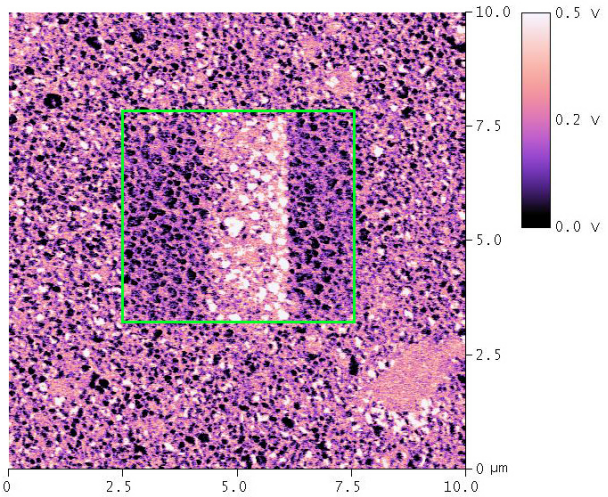

(c) Piezoresponse after poling with three alternate bands of +12 (white) and -12V (black).

Figure 5.11: PFM measurements on a (111) oriented substrate sample. (a) and (b) show the correlation between the topography and the PFM response, without any artificial poling: the BFO nanopillars offer good out-of-plane contrast and appear individually monodomain. Overall, a clear preferential polarization state can be seen. (c) shows the PFM image after poling with 1.5 μm wide stripe domains, which appear fully switched and stable after 24 hours.

polarization orientation over the whole region. After poling (figure 5.11(b)) with three 1.5 μm wide alternate bands of +12 (white) and -12V (black), all nanopillars appear fully polarized and stable after the 24 hours waiting time.

Furthermore, some of the surface aggregates discussed in the previous section exhibit ferroelectric behavior, as shown by larger scale measurements, which agrees with the fact, shown by SEM elemental analysis, that some of them are BFO precipitates. Figure 5.12 shows a set of PFM measurements performed on a $5 \times 5\mu m^2$ region on a (001) oriented substrate sample. The PFM response with no previous electrical poling, shown in figure 5.12(b), shows as before a polydomain polarization state, in particular in the large surface aggregates. On the far left aggregate, only the external 'ring', that appears lower on the AFM topography, exhibits a spontaneous polarization, indicating a different chemical composition. Figures 5.12(c) and 5.12(d) show PFM measurements of the same region after uniformly poling the region with -12 and +12 V respectively. The aggregates show a largely switched and stable polarization after 24 hours. One may notice the decreasing tip-sample interaction quality in the last measurement, due to the significant surface roughness, which may be responsible for the only partial switching of the polarization in some of the aggregates. No PFM measurements involving surface aggregates were performed on (111) oriented substrate samples.

As these surface aggregates exhibit pure phases from XRD and stable magnetic or ferroelectric behavior from local probe measurements, achieving a control over their growth conditions might be an interesting pathway to self-assembled nanostructures with either magnetic or ferroelectric properties.

5.4 Local probe evidence of magnetoelectric coupling

The main goal of this work focuses on obtaining evidence of a magnetoelectric coupling between the ferroelectric and the ferrimagnetic phases in the (001) oriented substrate sample by local probe techniques. This is done by poling an area of the film with the AFM tip, and by looking for magnetic domain switching in the ferrimagnetic phase, induced by the polarization switching in the ferroelectric phase (see details below). This experience was motivated by the work of Zavaliche et al., who showed evidence in ref. [11] of magnetic domain switching after electrical poling on similar samples, as shown on figure 5.13 from their article.

In this work, an attempt to obtain similar results was conducted as follow: first, the film was magnetized out-of-plane in a 2 T magnetic field, which results in a $\approx 75\%$ predominantly magnetized CFO nanopillars ratio (cf. figure 5.7). Second, the film was electrically poled with -12 V, and polarization switching in BFO was confirmed by PFM. The difference between the MFM images taken before and after electrical poling was then analyzed to identify magnetic domain swtiching solely due to electrical poling. The experience was then repeated with an electrical poling of +12 V.

Figures 5.14(b) and 5.14(c) show the MFM phase measurements before and after electrically poling the 3×3 μm^2 central region with -12 V (green square in figure 5.14(a)). Figures 5.14(d) and 5.14(e) show difference images between the two phase measurements, in regions corresponding respectively to the green and blue rectangles in figure 5.14(c). Indeed, as tip drift during scanning leads to artefacts in this identification method (the two images are not exactly superposed), different centering points are taken to accurately identify those magnetic domains

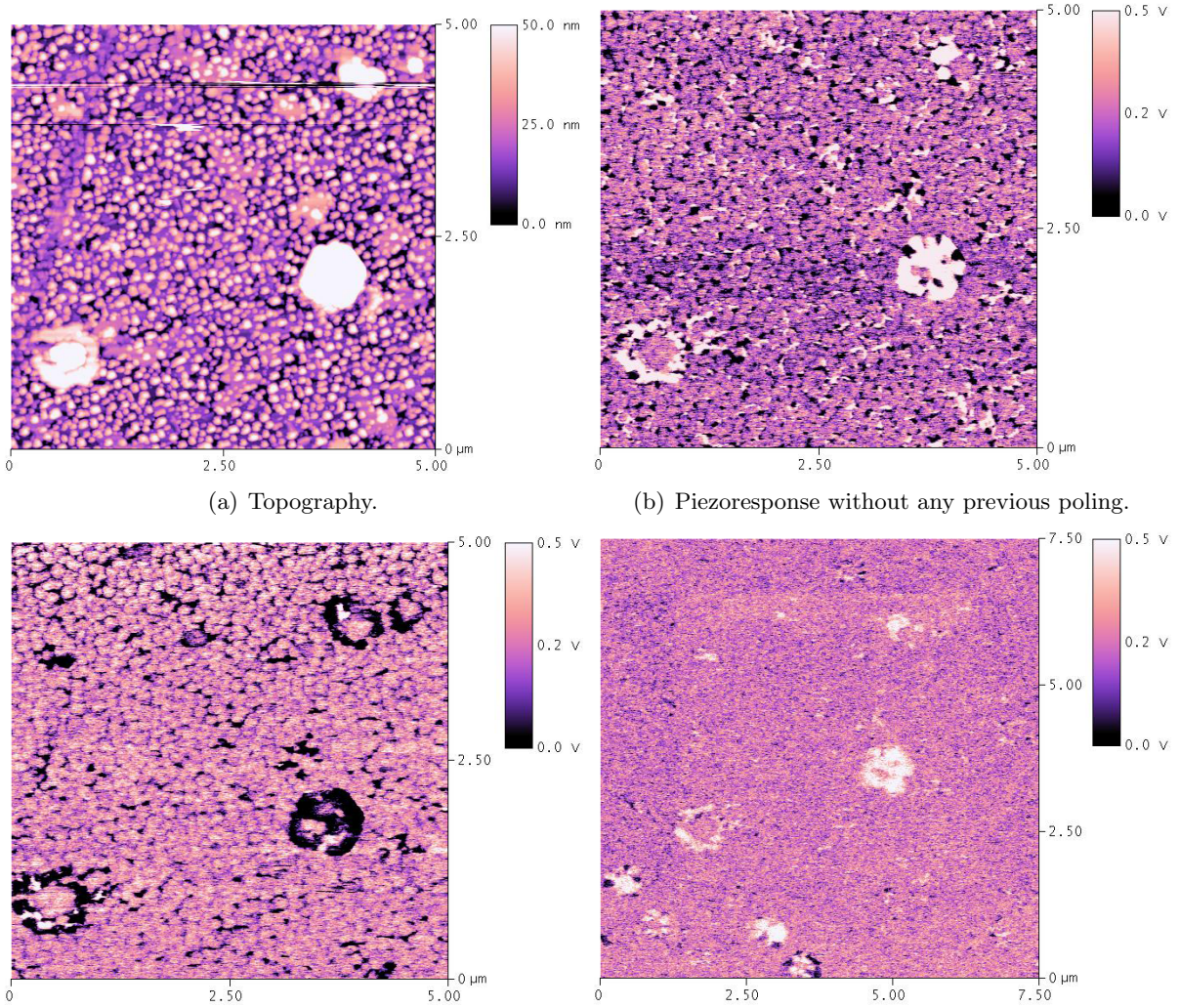

(a) Topography.

(b) Piezoresponse without any previous poling.

(c) Piezoresponse after poling uniformely with -12 V.

(d) Piezoresponse after poling uniformely with +12 V.

Figure 5.12: PFM measurements on a (001) oriented substrate sample, on a region involving large surface aggregates. (b) shows that some parts of the aggregates exhibit a spontaneous polydomain polarization state without any previous poling, similarly to the BFO matrix. (c) and (d) show that the BFO matrix and the aggregates are switched and stable after poling with -12 and +12 V respectively. Partial polarization switching in the aggregates may come from the degradating tip-sample interaction due to surface roughness.

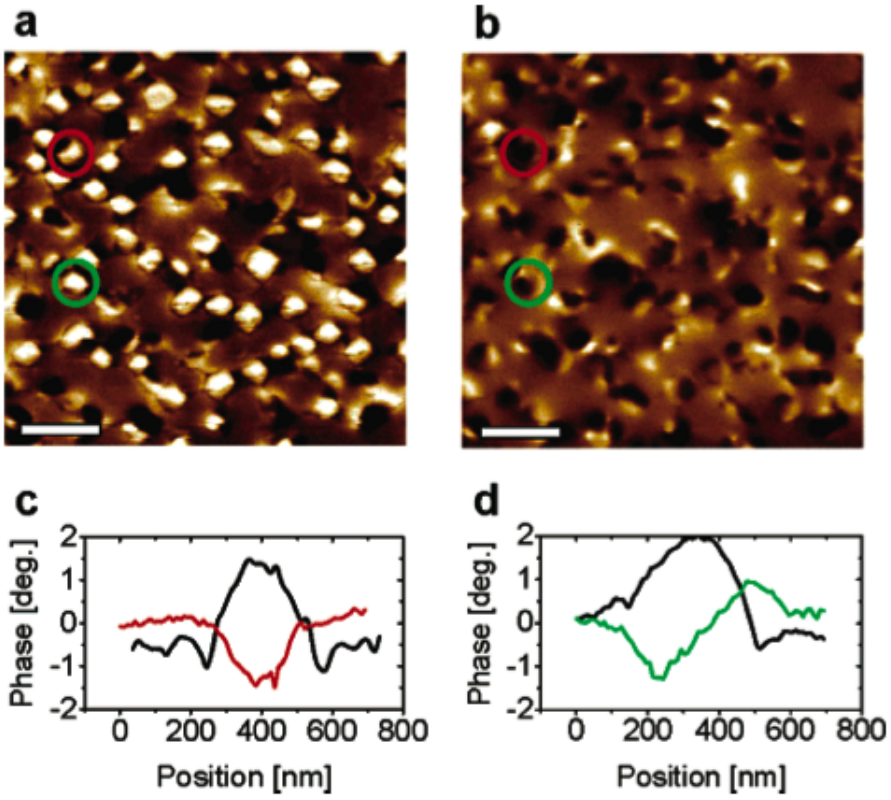

Figure 5.13: MFM imaging from ref. [11] after magnetization in a 2 T perpendicular field (a) and after electrical poling with +12 V (b). The line profiles shown in (c) and (d) show that one domain (in red) was fully reversed, while the other one (in green) was only partially reversed. The black curves stand for the MFM signal before electrical poling.

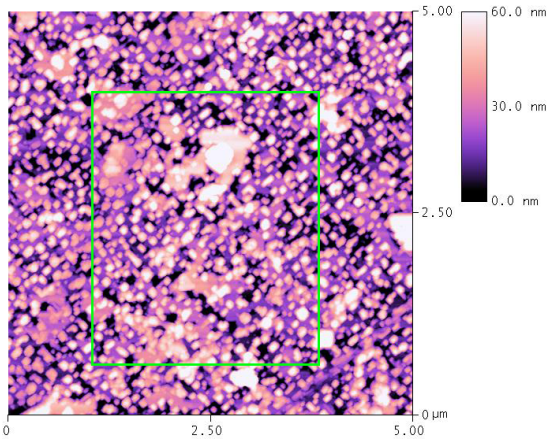

(a) Topography.

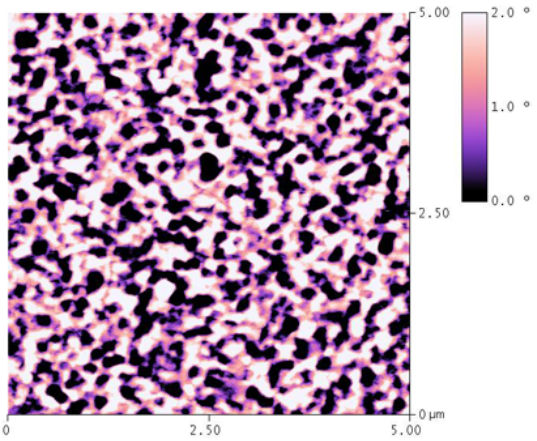

(b) MFM before electrical poling.

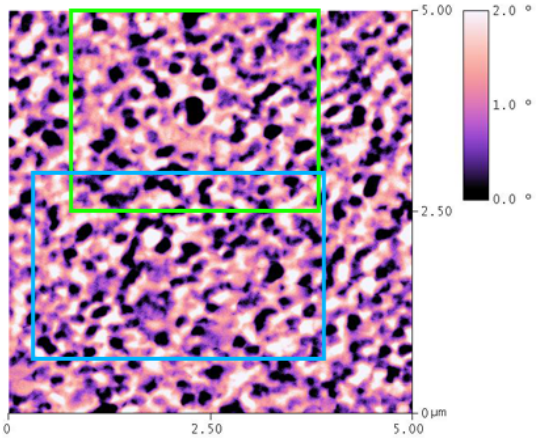

(c) MFM after electrical poling.

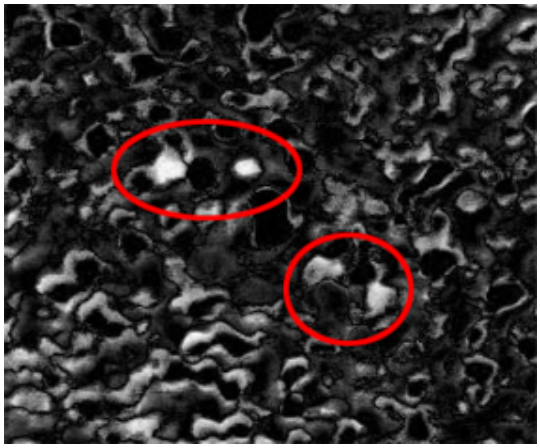

(d) Difference image corresponding the the green rectangle in 5.14(c) (arbitrary units).

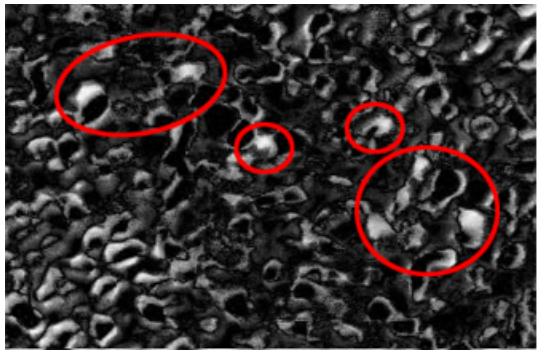

(e) Difference image corresponding the the blue rectangle in 5.14(c) (arbitrary units).

Figure 5.14: MFM measurements before and after electrical poling with -12 V on a (001) oriented substrate sample, showing the switching of magnetic domains. The phase scale is the same in 5.14(b) and 5.14(c) for quantitative analysis. Regions with different centering points are analyzed to eliminate artefacts due to tip drift during scanning.

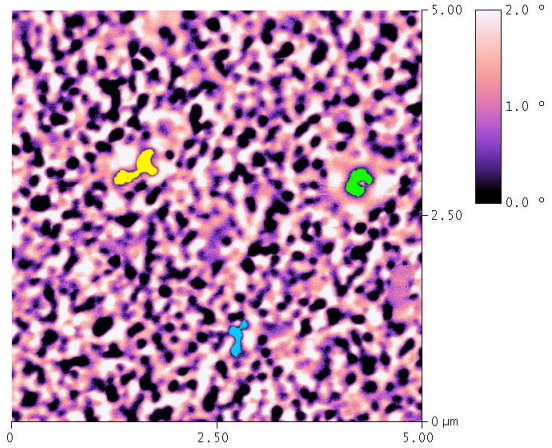

(a) MFM before electrical poling.

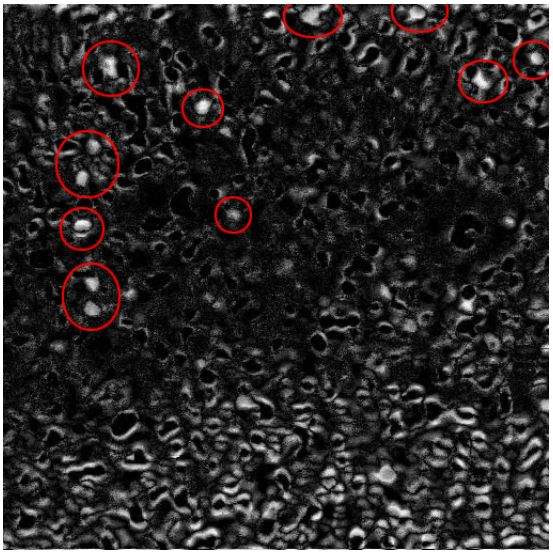

(b) Difference image centered around the yellow feature in 5.15(a) (arbitrary units).

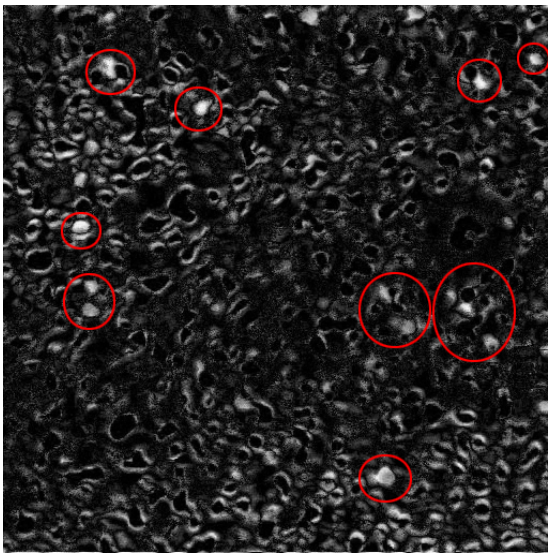

(c) Difference image centered around the green feature in 5.15(a) (arbitrary units).

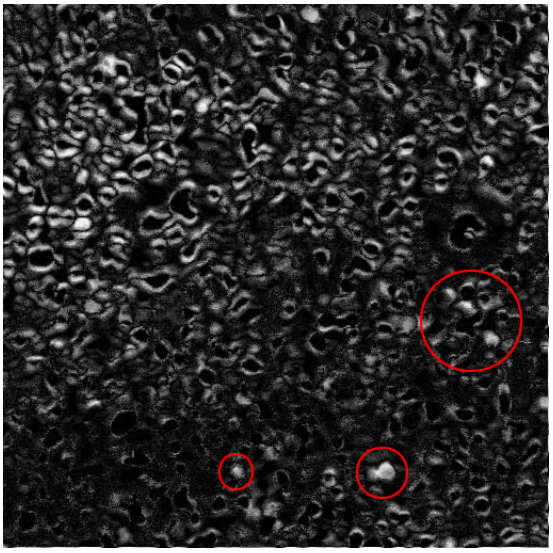

(d) Difference image centered around the blue feature in 5.15(a) (arbitrary units).

Figure 5.15: MFM measurements before and after electrical poling with +12 V on a (001) oriented substrate sample, showing switching magnetic domains. Again, different centering points are considered to differentiate the MFM measurements before and after electrical poling. The artefacts due to tip drift can be seen as white fringes (e.g. in the lower right corner in (b)).

which have switched as a result of electrical polarization reversal. From these measurments, we observe that a ratio of about $12 \pm 5\%$ of magnetic domains has been shown to switch magnetization after electrical poling, with the error margin estimated by taking an uncertainty of 10 nm along the poled region borders and a deviation due to unclear domains. Unfortunately, the complementary operation involving electrical poling with +12 V did not yield clear magnetic domain switching; the PFM measurement, however, did not show full switching of the electrical polarization in the BFO matrix.

A similar set of measurements is shown on figure 5.15 after electrically poling over the whole 5×5 μm^2 region with +12 V. The MFM phase image shown in figure 5.15(a), taken before electrical poling, shows in color the three centering points taken to identify switching magnetic domains, with corresponding difference images shown in figures 5.15(b), 5.15(c) and 5.15(c). The artefacts due to tip drift can be seen as white fringes, for instance in the lower right corner in figure 5.15(b). In this measurements, the resulting ratio of switching magnetic domains after electrical poling is found to be $14 \pm 5\%$.

5.5 Stochastic nature of the magnetization reversal under an applied electric field

In 2007, Zavaliche et al. showed that the effect of magnetization reversal under an applied electric field was stochastic in zero magnetic field in similar samples, in the framework of similar local probe magnetoelectric coupling studies (ref. [21]). Their samples were previously magnetized in up and down 2 T magnetic fields, and MFM measurements then showed a uniform out-of-plane nanopillar magnetization (in contrast to our $\sim 80\%$ ratio of preferentially magnetized nanopillars). For both magnetization states, MFM measurements then performed on regions electrically poled with -16 V showed a ratio of magnetic domains that had switched after electrical poling of $50 \pm 10\%$. The authors proposed a stochastic effect as a result of magnetoelectric coupling, which could explain the observed ratio (see figure 5.16).

Initially, the CFO nanopillars exhibit a perpendicular magnetic anisotropy (with an up magnetization in figure 5.16(a). As a perpendicular electric field is applied, the BFO matrix goes through a pseudocubic phase transition during polarization switching (figure 5.16b), which induces a compressive stress on the CFO matrix. Because CFO is highly magnetostrictive, the nanopillars exhibit an increased perpendicular magnetic anisotropy. Once the BFO polarization switches in one of the threee possible ways shown in figure 5.16(c), the nanopillars are subject to a tensile stress that induces a four-fold in-plane magnetic anisotropy. At this point, a spin reorientation from out-of-plane to in-plane may occur to minimize the anisotropy energy. Finally, as the electric field is removed (figure. 5.16(d), the tensile stress is relieved and the initial out-of-plane magnetic anisotropy takes over. The magnetization may therefore flip either up or down with equal probabilites, in agreement with the 50% ratio of nanopillars that reverse magnetization.

With an applied bias of +16 V under the same conditions, Zavaliche et al. showed a reversal of magnetization in $\sim 30\%$ of the nanopillars, which according to the magnetoelectric coupling mechanism proposed may be the result of less favorable stress dynamics.

Since in our samples a mean ratio of reversed nanopillars of $\sim 13\%$ was evidenced by MFM, this mechanism cannot alone be reponsible for magnetoelectric coupling in the nanostructure.

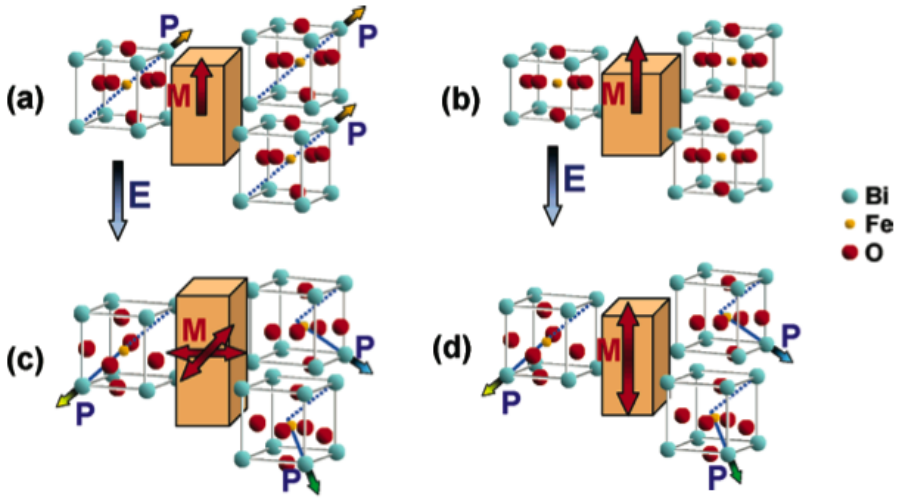

Figure 5.16: Sketch of magnetization reversal process in CFO due to polarization switching in the BFO matrix, adapted from ref. [21]. (a) Initial configuration with perpendicular magnetic anisotropy. (b) The transient pseudocubic distortion of the BFO matrix increases the perpendicular magnetic anisotropy due to compressive stress. (c) The tensile stress following from the polarization switching in BFO induces a four-fold in-plane magnetic anisotropy. The three possible ferroelectric switching mechanisms in BFO are depicted. (d) As the electric field is removed, the final configuration with perpendicular magnetic anisotropy has a 50% chance to return to its initial state or to reverse.

Chapter 6

Conclusion and outlook

In summary, we have presented topographic, magnetic and ferroelectric characterization, and evidence of magnetoelectric coupling in BFO-CFO nanocomposite thin films on Nb:STO substrates, grown by pulsed laser deposition in the group of J. Fontcuberta. In these films, one of the phases organizes into nanopillars embedded in the other phase, depending on the substrate crystallographic orientation. On (001) substrate oriented samples, CFO forms nanopillars in the BFO matrix, and conversely for (111) substrate oriented samples.

AFM topography shows an average rms surface roughness of ∼20 nm and a nanopillar faceting in agreement with FESEM measurements performed in the group of J. Fontcuberta. In addition, surface aggregates are observed, with either magnetic or ferroelectric behavior. An elemental analysis performed by SEM measurements shows these aggregates to be either CFO or BFO precipitates, in agreement with XRD measurments which do not show any other phases. The macroscopic magnetic measurements performed by SQUID show a coercive field of about 2 kOe and a remanent magnetization value coherent for both kinds of sample with local magnetic measurements performed by MFM. PFM preliminary measurements show that the ferroelectric phase exhibits a stable and switchable electrical polarization in both kinds of samples, under the form of matrix or nanopillars.

Evidence of strain-induced magnetoelectric coupling has been achieved in (001) substrate oriented samples, previously magnetized under a 20 kOe magnetic field. After switching the electrical polarization of the BFO matrix in a uniformely polarized region, magnetic domain switching has been observed by MFM in the CFO nanopillars. The average ratio of switching nanopillars is found to be $\approx 13 \pm 5\%$. This result does not fully agree with the stochastic mechanism proposed by Zavaliche et al. in ref. [21]. However, as the said mechanism is very strain dependent and is shown by the authors to be influenced by stress dynamics conditions, further studies about the role of epitaxial strain in the strength of the magnetoelectric coupling may provide additional information on the observed ratio.

Local probe studies on this kind of samples may be extended in future experiments to characterize possible polarization switching induced by a magnetic field, particularly in the (111) substrate oriented samples, in which the ferroelectric BFO forms the nanopillars embedded in the CFO matrix. Also, a study of the role of the epitaxial strain, for instance by investigating different types of substrates or by changing the BFO/CFO ratio, could lead to different amounts of magnetoelectric coupling effect.

Furthermore, it is possible that the surface-sensitive local probe techniques used in this study might not reflect the bulk behavior in the interior of the film. Measurements simutatneously accessing bulk magnetization and electrical polarization could provide additional information on the nature of the magnetoelectric coupling in this system.

Bibliography

[1] C. Kittel, Physique de l'état solide, 8ème édition, *Dunod* (2007).

[2] F. Duan and J. Guojun, Introduction to Condensed Matter Physics vol. 1, *World Scientific* (2005).

[3] J.M. Yeomans, Statistical Mechanics of Phase Transistions, *Oxford University Press* (2002).

[4] M. E. Lines and A. M. Glass, Principles and Applications of Ferroelectrics and Related Materials, Oxford University Press (2004).

[5] W. Eerenstein, N. D. Mathur and J. F. Scott, Multiferroic and magnetoelectric materials, *Nature* **442**, 759 (2006).

[6] R. Ramesh and N. A. Spaldin, Multiferroics : progress and prospects in thin films, *Nature materials* **6**, 21 (2007).

[7] N. A. Spaldin and M. Fiebig, The Renaissance of Magnetoelectric Multiferroics, *Science* **309**, 391 (2005).

[8] M. Fiebig, Revival of the magnetoelectric effect, *J. Phys. D: Appl. Phys.* **38** (2005).

[9] N. A. Hill, Why Are There so Few Magnetic Ferroelectrics?, *J. Phys. Chem. B* **2000**, *104*, 6694-6709 (2000).

[10] S.-W. Cheong and M. Mostovoy, Multiferroics: a magnetic twist for ferroelectricity, *Nature materials* **6**, 13 (2007).

[11] F. Zavaliche *et al.*, Electric Field-Induced Magnetization Switching in Epitaxial Columnar Nanostructures, *Nano Lett.* **5**, 1793-1796 (2005).

[12] W. F. Jr Brown, R. M. Hornreich and S. Shtrikman, Upper bound on the magnetoelectric susceptibility, *Phys. Rev.* **168**, 743-577 (1968).

[13] B. B. Van Aken, J.-P. Rivera, H. Schmid and M. Fiebig, Observation of ferrotoroidic domains, *Nature* **449**, 702-704 (2007).

[14] K. Rabe, Response with a twist, *Nature* **449**, 674-675 (2007).

[15] H. Zhen *et al.*, Multiferroic $BaTiO_3$-$CoFe_2O_4$ nanostructures, *Science* **303**, 661-663 (2004).

[16] C. Michel, J.-M. Moreau, G. D. Achenbach, R. Gerson and W. J. James, The atomic structure of $BiFeO_3$, Solid State Comm. **7**, 701-704 (1969).

[17] D. Lebeugle, D. Colson, A. Forget and M. Viret, Very large spontaneous electric polarization in $BiFeO_3$ single crystals at room temperature and its evolution under cycling fields, *Appl. Phys. Lett.* **91**, 022907 (2007).

[18] C. Ederer and N. A. Spaldin, Weak ferromagnetism and magnetoelectric coupling in bismuth ferrite, Phys. Rev. B **71**, 060401 (R) (2005).

[19] R. Muralidharan *et al.*, Synthesis, structure and magnetic studies on self-assembled $BiFeO_3$-$CoFe_2O_4$ nanocomposites thin films, *Journal of Appl. Phys.* **103**, 07E301 (2008).

[20] A. Berkowitz and W. J. Schuele, Magnetic Properties of Some Ferrite Micropowders *J. Appl. Phys.* **30**, S134 (1959).

[21] F. Zavaliche *et al.*, Electrically Assisted Magnetic recording in Multiferroic Nanosctructures, *Nano Lett.* **7**, 1586-1590 (2007).